Amplitude analysis of the $\Lambda_c^+ \to pK^-\pi^+$ decay and Λ_c^+ baryon polarization measurement in semileptonic beauty hadron decays

R. Aaij *et al.*[*]
(LHCb Collaboration)

(Received 6 August 2022; accepted 3 October 2022; published 28 July 2023)

An amplitude analysis of $\Lambda_c^+ \to pK^-\pi^+$ decays together with a measurement of the Λ_c^+ polarization vector in semiōleptonic beauty hadron decays is presented. A sample of 400 000 candidates is selected from proton-proton collisions recorded by the LHCb detector at a center-of-mass energy of 13 TeV. An amplitude model is developed and the resonance fractions as well as two- and three-body decay parameters are reported. The mass and width of the $\Lambda(2000)$ state are also determined. A significant Λ_c^+ polarization is found. A large sensitivity of the $\Lambda_c^+ \to pK^-\pi^+$ decay to the polarization is seen, making the amplitude model suitable for Λ_c^+ polarization measurements in other systems.

DOI: 10.1103/PhysRevD.108.012023

I. INTRODUCTION

The $\Lambda_c^+ \to pK^-\pi^+$ decay has a complex resonant structure, with multiple overlapping states in the $K^-\pi^+$, pK^- and $p\pi^+$ systems. A full amplitude analysis is therefore necessary to determine the composition of the decay amplitude, allowing the determination of the Λ_c^+ polarization, as described in Ref. [1]. The developed $\Lambda_c^+ \to pK^-\pi^+$ amplitude model therefore has multiple applications ranging from new physics searches to low-energy QCD studies.

The helicity amplitudes characterize each contribution to the $\Lambda_c^+ \to pK^-\pi^+$ decay, including intermediate state polarization. In general, the knowledge of the resonant structure is useful in searches for CP symmetry violation, which are still unobserved in baryon decays, and can be related to specific contributions or localized in phase space. Parity violation is characterized by the decay asymmetry α parameters associated to the two-body resonant contributions, which are determined from the helicity couplings. In this respect, the prediction of the parity-conserving nature of $1/2^+ \to 3/2^+0^-$ decays [2] can be tested. Parity violation is also studied for the entire three-body $\Lambda_c^+ \to pK^-\pi^+$ process, considering a quantity called average event information [3], which represents the sensitivity of the decay to the baryon polarization.

The $\Lambda_c^+ \to pK^-\pi^+$ decay amplitude can be exploited in studies of $\Lambda_b^0 \to \Lambda_c^+ l^- \bar{\nu}_l$ decays, in which the possibility to analyze the spin of the Λ_c^+ baryon increases the sensitivity to possible contributions beyond the Standard Model [4–18]. Such analyses are motivated by the anomalies seen in $b \to cl\nu$ processes [19–24] but are also interesting for Cabibbo-Kobayashi-Maskawa matrix angle measurements and CP-violation searches.

The $\Lambda_c^+ \to pK^-\pi^+$ amplitude model can be employed to measure the polarization of the Λ_c^+ baryon. This Λ_c^+ decay mode is particularly suited thanks to its good reconstruction efficiency, through the vertexing of three charged, displaced tracks. For comparison, the two-body decay $\Lambda_c^+ \to \Lambda\pi^+$, usable for polarization measurements since its decay asymmetry parameter is known [25], has a lower branching fraction by a factor of about 5 [25] and a reduced detector reconstruction efficiency because of the large Λ baryon flight distance.

The measurement of the Λ_c^+ polarization has been advocated for many production processes: Λ_b^0 semileptonic decays, for which several theoretical predictions are available [6,9,10,15,18,26,27]; weak interaction vector boson decays [28,29] and strong interactions [28,30,31]. Polarization measurements of Λ_c^+ baryons are a fundamental probe of their spin structure and formation process via hadronization of heavy charm quarks. According to the heavy quark effective theory, most of the c-quark polarization is expected to be retained by the charm baryon [28,29,32]. In the case of strong force production, the baryon polarization is difficult to predict in the nonperturbative regime of QCD, its measurement discriminates among different low-energy QCD approaches. The Λ_c^+ polarization also constitutes an additional probe for new physics effects. Its measurement can complement the aforementioned $b \to cl\nu$ angular analyses providing an additional observable to test. Moreover, it enables the measurement of charm baryon electric and magnetic dipole moments via spin precession [33–36].

[*]Full author list given at the end of the article.

In this paper, an amplitude analysis of $\Lambda_c^+ \to pK^-\pi^+$ decays recorded by the LHCb detector is presented. Charge conjugate states are implied. The analysis is based on a data sample of semileptonic decays of beauty hadrons produced in proton-proton (pp) collisions at a center-of-mass energy of 13 TeV, recorded in 2016, corresponding to an integrated luminosity of 1.7 fb^{-1}. A high purity sample of 400 000 candidates is selected for the amplitude fit. This $\Lambda_c^+ \to pK^-\pi^+$ amplitude analysis improves the measurement performed by the E791 experiment at Fermilab [37] by increasing the size data sample by a factor ≈400 and addressing the recently realized issue of the matching of proton spin states among different decay chains [38].

This paper is organized as follows. The description of the LHCb detector and the simulation sample employed is given in Sec. II. The selection of $\Lambda_c^+ \to pK^-\pi^+$ candidates and the invariant mass fit used to determine signal and background yields are described in Sec. III. The amplitude analysis framework and the development of the $\Lambda_c^+ \to pK^-\pi^+$ default amplitude model are described in Sec. IV. The evaluation of statistical and systematic uncertainties is covered by Sec. V, along with the consistency checks performed. The results of the amplitude fit are reported in Sec. VI, and a brief summary of the amplitude analysis is provided in Sec. VII. Appendix A presents the building of the $\Lambda_c^+ \to pK^-\pi^+$ amplitude model in the helicity formalism following the method for the matching of the proton spin of Ref. [38], along with the definition of the Λ_c^+ polarization systems employed and the description of the $\Lambda_c^+ \to pK^-\pi^+$ phase space.

II. DETECTOR AND SIMULATION

The LHCb detector [39,40] is a single-arm forward spectrometer covering the pseudorapidity range $2 < \eta < 5$, designed for the study of particles containing b or c quarks. The detector includes a high-precision tracking system consisting of a silicon-strip vertex detector surrounding the pp interaction region, a large-area silicon-strip detector located upstream of a dipole magnet with a bending power of about 4 Tm, and three stations of silicon-strip detectors and straw drift tubes placed downstream of the magnet. The tracking system provides a measurement of the momentum, p, of charged particles with a relative uncertainty that varies from 0.5% at low momentum to 1.0% at 200 GeV. Natural units with $c = 1$ are used throughout. The minimum distance of a track to a primary pp collision vertex (PV), the impact parameter, is measured with a resolution of $(15 + 29/p_{\mathrm{T}})$ μm, where p_{T} is the component of the momentum transverse to the beam, in GeV. Different types of charged hadrons are distinguished using information from two ring-imaging Cherenkov detectors. Photons, electrons and hadrons are identified by a calorimeter system consisting of scintillating-pad and preshower detectors, an electromagnetic and a hadronic calorimeter. Muons are identified by a system composed of alternating layers of iron and multiwire proportional chambers. The online event selection is performed by a trigger, which consists of a hardware stage, based on information from the calorimeter and muon systems, followed by a software stage, which applies a full event reconstruction.

At the hardware trigger stage, events are required to have at least one muon with high p_{T}. The software trigger requires a two-, three- or four-track secondary vertex with a significant displacement from any primary pp interaction vertex. At least one charged particle must have a transverse momentum $p_{\mathrm{T}} > 1.6$ GeV and be inconsistent with originating from a PV. A multivariate algorithm [41,42] is used for the identification of secondary vertices consistent with the decay of a b hadron.

The momentum scale is calibrated using samples of $J/\psi \to \mu^+\mu^-$ and $B^+ \to J/\psi K^+$ decays collected concurrently with the data sample used for this analysis [43,44]. The relative accuracy of this procedure is estimated to be 3×10^{-4} using samples of other b hadrons, Υ and K_{S}^0 mesons.

Simulation is required to model the effects of the detector acceptance and the imposed selection requirements. In the simulation, pp collisions are generated using PYTHIA [45] with a specific LHCb configuration [46]. Decays of unstable particles are described by EVTGEN [47], in which final-state radiation is generated using PHOTOS [48]. The interaction of the generated particles with the detector, and its response, are implemented using the Geant4 toolkit [49] as described in Ref. [50]. The underlying pp interaction is reused multiple times, with an independently generated signal decay for each [51].

Simulated $\Lambda_b^0 \to \Lambda_c^+\mu^-\bar{\nu}_\mu$ decays are produced with the $\Lambda_c^+ \to pK^-\pi^+$ decay uniformly generated over the phase space. This sample consists of about 450 000 events passing the selection criteria.

The particle identification (PID) response in the simulated samples is calibrated by sampling from distributions of $D^{*+} \to D^0\pi^+$, $D^0 \to K^-\pi^+$ and $\Lambda_b^0 \to \Lambda_c^+\pi^-$, $\Lambda_c^+ \to pK^-\pi^+$ decays, considering their kinematics and the detector occupancy. An unbinned method is employed, where the probability density functions are modeled using kernel density estimation [52]. The Λ_c^+ momentum and transverse momentum distributions in the simulated samples are corrected in order to reproduce the data distribution using the gradient boost weighting technique of the `hep_ml` package [53].

III. SELECTION AND INVARIANT MASS FIT

The data sample used in this analysis corresponds to an integrated luminosity of 1.7 fb^{-1}. The Λ_c^+ candidates are reconstructed from combinations of three charged hadron tracks forming a vertex separated from the PV. Semileptonic beauty hadron decay candidates are then reconstructed inclusively requiring that the Λ_c^+ candidate

and a muon track originate from a common vertex. Small χ^2 values are required for all track and vertex fits. Each track is required to have a good particle identification response, transverse momentum $p_T > 250$ MeV for hadrons and $p_T > 1$ GeV for muons and momentum $p > 2$ GeV for mesons, $p > 8$ GeV for protons and $p > 6$ GeV for muons. Final-state particles are ensured to be well displaced from the interaction point by requiring a large track χ^2_{IP} with respect to any PV, where χ^2_{IP} is defined as the difference in the vertex fit χ^2 of a given PV reconstructed with and without the particle under consideration. The associated PV is the one featuring the smallest χ^2_{IP}.

Further selection criteria are used to reduce the combinatorial background contamination to roughly 1%. Strict requirements are imposed on proton and kaon particle identification probabilities, obtained from neural network classifiers, which combine information from the different subdetectors. Probabilities larger than 0.95 and 0.7 are selected for proton and kaon hypotheses, respectively. The $\Lambda_c^+\mu^-$ vertex is required to be significantly displaced from the PV, displacement measured in terms of a χ^2 test. A maximum distance along the beam axis between $\Lambda_c^+\mu^-$ and $pK^-\pi^+$ vertexes of 6 mm is also imposed. The only physical sources of background identified before applying the aforementioned selection criteria, $D^+ \to K^-\pi^+\pi^+$ and $D_s^+ \to K^+K^-\pi^+$ decays, are effectively rejected by the tight proton identification requirement. No specific vetoes are therefore applied.

The distribution of the invariant mass $m(pK^-\pi^+)$ of selected $pK^-\pi^+$ candidates from the total dataset is shown in Fig. 1. An extended unbinned maximum-likelihood fit is performed to the $m(pK^-\pi^+)$ distribution in the mass range within 80 MeV of the known Λ_c^+ mass [25]. The $\Lambda_c^+ \to pK^-\pi^+$ signal component is modeled with a double-sided Crystal Ball function [54], having asymmetric power-law tails on both sides of the peak to describe

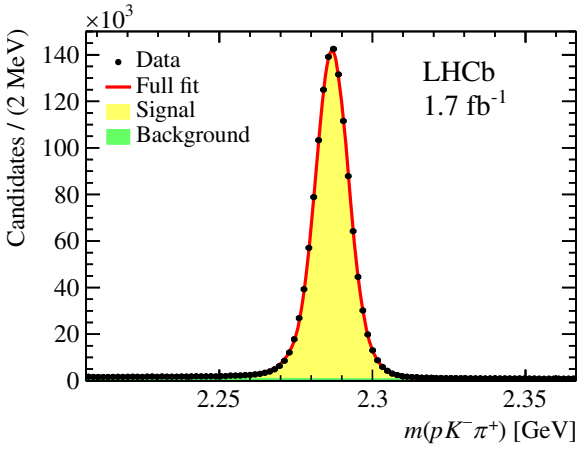

FIG. 1. Invariant mass distribution of selected $pK^-\pi^+$ candidates from the total dataset. The results from the fit described in the text are also shown.

detector resolution and final-state radiation effects. An exponential function describes the combinatorial background contribution.

The signal $m(pK^-\pi^+)$ region chosen for the amplitude analysis is within 15 MeV of the known Λ_c^+ mass [25], containing about 95% of the signal candidates. The fraction of background in the signal region is $f_b = 1.69\%$.

A subset of 400 000 $\Lambda_c^+ \to pK^-\pi^+$ candidates is employed, corresponding to roughly 30% of the analyzed dataset, since increasing the dataset does not reduce the leading source of systematic uncertainty (see Sec. V). The subset is chosen selecting an equal number of candidates per each category of Λ_c^+ baryon charge and LHCb magnet polarity.

IV. AMPLITUDE FIT

The amplitude model for the $\Lambda_c^+ \to pK^-\pi^+$ decay is written in the helicity formalism [55], following the method and conventions of Ref. [38]. In particular, the method for the matching of the proton spin among different decay chains is employed. The Λ_c^+ polarization is measured in the Λ_c^+ rest frame in two different helicity systems defined by a boost along the Λ_c^+ momentum from the laboratory frame (*lab*), and from the approximate beauty hadron rest frame ($\tilde{B}$). The five variables describing the $\Lambda_c^+ \to pK^-\pi^+$ decay are chosen to be

$$\Omega = (m^2_{pK^-}, m^2_{K^-\pi^+}, \cos\theta_p, \phi_p, \chi), \tag{1}$$

where $m^2_{pK^-}$ and $m^2_{K^-\pi^+}$ are the squared invariant masses and θ_p, ϕ_p and χ are the angles describing the decay orientation with respect to the Λ_c^+ polarization system. The angles θ_p and ϕ_p are the polar and azimuthal angles of the proton momentum, while χ is the angle between the plane formed by the proton momentum and the Λ_c^+ quantization axis and the plane formed by the kaon and pion momenta, where momenta are expressed in the Λ_c^+ rest frame. The detailed definition of the amplitude model, Λ_c^+ helicity systems and phase-space variables is given in Appendix A.

The free parameters of the amplitude model, denoted ω, are determined by an unbinned maximum-likelihood fit to the five phase-space observables Ω, defined in Eq. (1), with ω including helicity couplings, line shape parameters and polarization components. The negative logarithmic likelihood (NLL) minimized in the fit is

$$-\log\mathcal{L}(\omega) = -\sum_{i=1}^{N} \log p_{\rm tot}(\Omega_i|\omega), \tag{2}$$

where N is the number of events, with the probability density function (PDF)

$$p_{\rm tot}(\Omega_i|\omega) = \frac{p(\Omega_i|\omega)\epsilon(\Omega_i)}{I(\omega)}(1-f_b) + p_{\rm bkg}(\Omega_i)f_b, \quad (3)$$

which includes the $\Lambda_c^+ \to pK^-\pi^+$ decay rate $p(\Omega|\omega)$, the detector efficiency $\epsilon(\Omega)$ and the background contribution $p_{\rm bkg}(\Omega)$. The background fraction f_b is fixed to that determined from the $m(pK^-\pi^+)$ invariant mass fit, while $I(\omega)$ is the normalization of the signal part of the total PDF,

$$I(\omega) = \int p(\Omega|\omega)\epsilon(\Omega)d\Omega, \quad (4)$$

computed numerically using simulated events reconstructed through the detector. The phase-space variables Ω are computed after constraining the mass of the $pK^-\pi^+$ candidate to the known Λ_c^+ mass [25].

Equation (2) can be rewritten as

$$-\log\mathcal{L}(\omega) = -\sum_{i=1}^{N}\log\left[p(\Omega_i|\omega) + \frac{f_b}{1-f_b}\frac{p_{\rm bkg}(\Omega_i)I(\omega)}{\epsilon(\Omega_i)}\right] + N\log I(\omega) + \text{constant}. \quad (5)$$

Efficiency and background parametrizations are expressed in terms of factorized Legendre polynomial expansions, derived from simulation and data sidebands, respectively. They are described in Appendix C.

The amplitude fitting code is based on a version of the TensorFlowAnalysis package [56] adapted to three-body amplitudes in five-dimensional phase-space fits [35]; this package depends on the machine-learning framework TensorFlow [57] interfaced with MINUIT minimization [58] via the ROOT package [59]. The fit is performed using multiple gradient-descent minimization with different, randomized, initial values of the parameters, choosing the result with minimum NLL. This ensures that the global NLL minimum is reached.

The fit quality is measured by a χ^2 test performed over a five-dimensional binning of the phase space; an adaptive binning technique is employed to guarantee a similar number of candidates in each bin. Probability values are obtained assuming a number of degrees of freedom equal to the number of bins employed subtracted by the number of free parameters in the amplitude fit, including normalization.

The normalization of the model, Eq. (4), is determined by setting one of the helicity coupling values, defined in Eq. (A5) of Appendix A, to unity, with the value of the other couplings expressed relative to this reference. The $\mathcal{H}^{K^*(892)}_{1/2,0}$ helicity coupling is chosen as reference. The default model is obtained from the amplitude fit in which the Λ_c^+ polarization is expressed in the helicity system reached from the laboratory frame.

The fit fraction, FF, for each resonance R is obtained by computing the integral of the amplitude model over the phase space where only the R contribution is left. Fit fractions are normalized to the complete amplitude model integral, see Appendix A for a detailed definition. For each two-body contribution, the associated decay asymmetry parameter α is measured. It characterizes the two-body decay angular distribution,

$$\frac{d\Gamma}{d\cos\theta_R} \propto \frac{1}{2}(1+\alpha P\cos\theta_R), \quad (6)$$

in which $\cos\theta_R = \hat{\boldsymbol{P}}\cdot\hat{\boldsymbol{p}}(R)$ is the cosine of the angle between the polarization vector $\boldsymbol{P}$, its modulus denoted by P, and the direction of the intermediate resonance in the Λ_c^+ rest frame $\hat{\boldsymbol{p}}(R)$. The α parameters can be expressed as a combination of helicity coupling squared moduli: for a Λ_c^+ weak decay to a pair of states with spin J and 0 (for Λ, Δ, K^* spin zero intermediate states) it is

$$\alpha = \frac{|\mathcal{H}_{1/2,0}|^2 - |\mathcal{H}_{-1/2,0}|^2}{|\mathcal{H}_{1/2,0}|^2 + |\mathcal{H}_{-1/2,0}|^2}. \quad (7)$$

In light of the application of the $\Lambda_c^+ \to pK^-\pi^+$ amplitude model as a Λ_c^+ polarization analyzer, it is important to give a quantitative estimation of the sensitivity to the baryon polarization given by the decay. The sensitivity is related to the amount of parity violation in the decay; for instance, a parity conserving decay has no sensitivity to the decaying baryon polarization. The sensitivity is studied in comparison to that given by two-body decays, for which the sensitivity is given by the decay asymmetry parameter.

The sensitivity to polarization of the decay can be measured by the average event information, S^2, evaluated at zero polarization, which, for a given number of events N, is inversely proportional to the variance σ^2 of the polarization measurement,

$$S^2 = \frac{1}{N\sigma^2} = \left\langle\frac{g^2}{f^2}(\Omega)\right\rangle = \int\frac{g^2}{f}(\Omega)d\Omega, \quad (8)$$

(see Refs. [3,35,36]) with $f(\Omega)$, $g(\Omega)$ obtained expressing the decay rate PDF Eq. (A31) of Appendix A as

$$p_{\rm PDF}(\Omega|P_z) = f(\Omega) + P_z g(\Omega), \quad (9)$$

where the choice of the polarization direction is arbitrary, thanks to rotational invariance. Indeed, S^2 does not depend on the polarization direction. In practice, direction-dependent sensitivities could be induced by experimental effects, since detector efficiencies are usually not isotropic. The average event information for a two-body decay is related to the decay asymmetry parameter α as, applying Eqs. (6)–(8),

$$S = \frac{|\alpha|}{\sqrt{3}}, \quad (10)$$

so that the modulus of α can be seen as a measure of the polarization sensitivity. The sensitivity to the polarization of the $\Lambda_c^+ \to pK^-\pi^+$ three-body decay is obtained from Eq. (8) using its amplitude model. Like two-body decay asymmetry parameters, S^2 is a measure of parity violation, which ranges between zero (parity conservation) and $1/3$ (maximum parity violation). For an easier comparison to two-body decays, the sensitivity to polarization is expressed as $\sqrt{3}S$, which ranges between zero and unity.

For Λ_c^+ quasi-two-body decays to a pair of baryon and pseudoscalar, the $\sqrt{3}S$ quantity is equal to the absolute value of the α decay parameter computed via Eq. (7). For the $K^*(892)$ contribution, characterized by a different spin structure, the $\sqrt{3}S$ quantity is considered.

The Dalitz plot of the total reconstructed $\Lambda_c^+ \to pK^-\pi^+$ sample is presented in Fig. 2. The plot contains candidates from the signal region prior to efficiency correction. It displays a rich structure with resonant contributions from all three possible pairs of final state particles: $\Lambda \to pK^-$ resonances are visible as vertical bands, $K^* \to K^-\pi^+$ as horizontal bands and $\Delta^{++} \to p\pi^+$ as diagonal bands. The different intensity patterns can be explained by the spin of the resonance, by interference patterns or nonuniform detector efficiency. Regarding the Λ pattern, there are two narrow structures corresponding to $\Lambda(1520)$ and $\Lambda(1670)$ resonances, plus broader bands indicating possible $\Lambda(1405)$ and $\Lambda(1600)$ contributions. The only other vertical band is in the $m^2_{pK^-}$ region 3.8–4.0 GeV, where no clear resonances are reported according to Ref. [25]. Regarding K^* resonances, the clear band is due to the $K^*(892)$ meson. Higher-mass resonances, having pole masses outside the allowed phase space, may contribute thanks to the lower-mass tail of their broad distribution, possibly explaining the presence of an enhanced number of events at high $m^2_{K^-\pi^+}$. Even if a spin-zero nonresonant component cannot be excluded visually, the center of the Dalitz plot is almost empty of events. Finally, besides the apparent diagonal band due to the $\Delta(1232)^{++}$ resonance, there is a slightly enhanced diagonal band at higher $m^2_{p\pi^+}$ mass, a possible sign of additional Δ^{++} resonances. The Dalitz plot shows interference effects among resonances belonging to different decay chains, which are needed for the simultaneous measurement of helicity amplitudes and Λ_c^+ polarization vector [1]. It can be noted that the $K^*(892)$ band gets shifted when crossing the $\Lambda(1670)$ contribution, while the $\Lambda(1520)$ band shows a destructive interference pattern with high mass K^* contributions at the upper corner of the Dalitz plot.

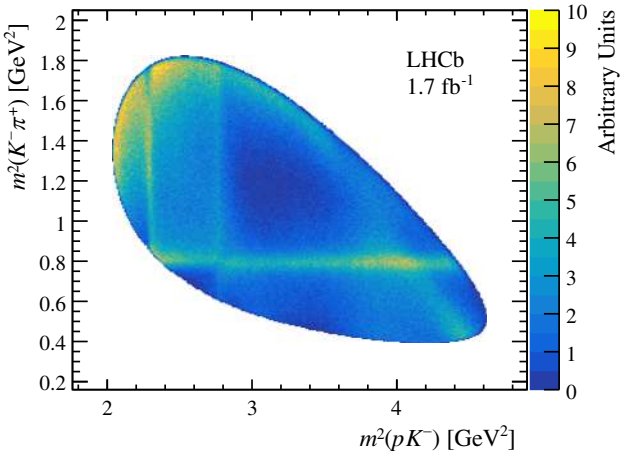

FIG. 2. Dalitz plot for the total sample of $\Lambda_c^+ \to pK^-\pi^+$ candidates.

The default amplitude model is built starting from the contributions visible in Fig. 2 and adding resonant states according to those listed in Ref. [25]. Contributions which significantly improve the fit quality are added to the default model; those giving similar qualities are considered as alternative models for systematic uncertainty evaluation. The same criterion is employed for choosing among different descriptions of the same contribution.

The resonances included in the default model are listed in Table I. Most resonance parameters are fixed to the mean values reported in Ref. [25]. The parameters of the broad $\Lambda(1600)$, $\Delta(1600)^{++}$, $\Delta(1700)^{++}$ and $K_0^*(1430)$ contributions are set to the edges of the intervals quoted by Ref. [25] giving better fit quality. These are the upper values of the $\Lambda(1600)$ and $\Delta(1600)^{++}$ masses, the lower values of the $\Delta(1700)^{++}$ and $K_0^*(1430)$ masses, the upper values of the $\Lambda(1600)$, $\Delta(1600)^{++}$, $\Delta(1700)^{++}$ widths and the lower value of the $K_0^*(1430)$ width. The mass and width of the narrow $\Lambda(1520)$ state are left free to absorb resolution effects. A large contribution from a resonant state in the $m(pK^-) \approx 2$ GeV region is observed and it is well described as a single $J^P = 1/2^-$ state,

TABLE I. Resonant composition of the default $\Lambda_c^+ \to pK^-\pi^+$ amplitude model, with spin-parity J^P, and the Breit-Wigner mass and width parameters, which, in the amplitude fit, are left free within the reported range or fixed to the given value if no interval is quoted.

Resonance	J^P	Mass (MeV)	Width (MeV)
$\Lambda(1405)$	$1/2^-$	1405.1	50.5
$\Lambda(1520)$	$3/2^-$	1515–1523	10–20
$\Lambda(1600)$	$1/2^+$	1630	250
$\Lambda(1670)$	$1/2^-$	1670	30
$\Lambda(1690)$	$3/2^-$	1690	70
$\Lambda(2000)$	$1/2^-$	1900–2100	20–400
$\Delta(1232)^{++}$	$3/2^+$	1232	117
$\Delta(1600)^{++}$	$3/2^+$	1640	300
$\Delta(1700)^{++}$	$3/2^-$	1690	380
$K_0^*(700)$	0^+	824	478
$K^*(892)$	1^-	895.5	47.3
$K_0^*(1430)$	0^+	1375	190

indicated as $\Lambda(2000)$, with Breit-Wigner parameters determined from the fit. Different spin-parity assignments are rejected by the fit.

The invariant mass dependence (line shape) of resonant contributions is parametrized by default with relativistic Breit-Wigner functions, whose implementation is described in Appendix D. Some of the resonances employed in the amplitude model cannot be parametrized by relativistic Breit-Wigner line shapes. The spin-zero contribution in the K^* decay channel is modeled as $K_0^*(700)$ and $K_0^*(1430)$ resonant states, each described by a simplified version of the parametrization proposed in Ref. [60]. It consists of a Breit-Wigner line shape, Eq. (D1), in which the mass-dependent width is given by

$$\Gamma(m) = \frac{m^2 - s_A}{m_0^2 - s_A}\Gamma_0 e^{-\gamma m^2}, \tag{11}$$

which features a singularity (Adler zero) at $s_A = m_K^2 - 0.5m_\pi^2$ and an exponential form factor on the $K\pi$ width driven by the parameter γ. The γ parameter is left free separately for each contribution. Comparing this line shape to the parametrization presented in Ref. [60], the additional overall exponential form factor $\exp[-\alpha q^2(m)]$, with $q(m)$

TABLE II. Systematic uncertainty contributions on fit parameters describing the Λ contributions. Total* includes all contributions except for the choice of the amplitude model.

Parameter	Model choice	Total*	Background	Kinematics	PID	Fit bias
$\mathrm{Re}\mathcal{H}_{1/2,0}^{\Lambda(1405)}$	3.3	0.1	0.0	0.0	0.0	0.0
$\mathrm{Im}\mathcal{H}_{1/2,0}^{\Lambda(1405)}$	3.2	0.1	0.1	0.0	0.1	0.0
$\mathrm{Re}\mathcal{H}_{-1/2,0}^{\Lambda(1405)}$	12	0.2	0.1	0.1	0.0	0.1
$\mathrm{Im}\mathcal{H}_{-1/2,0}^{\Lambda(1405)}$	3.7	0.3	0.2	0.1	0.2	0.0
$\mathrm{Re}\mathcal{H}_{1/2,0}^{\Lambda(1520)}$	0.12	0.01	0.00	0.00	0.00	0.00
$\mathrm{Im}\mathcal{H}_{1/2,0}^{\Lambda(1520)}$	0.12	0.02	0.01	0.00	0.01	0.00
$\mathrm{Re}\mathcal{H}_{-1/2,0}^{\Lambda(1520)}$	0.69	0.03	0.01	0.02	0.02	0.00
$\mathrm{Im}\mathcal{H}_{-1/2,0}^{\Lambda(1520)}$	1.3	0.0	0.0	0.0	0.0	0.0
$m^{\Lambda(1520)}$ [MeV]	0.65	0.03	0.03	0.01	0.01	0.01
$\Gamma^{\Lambda(1520)}$ [MeV]	1.3	0.1	0.1	0.1	0.1	0.0
$\mathrm{Re}\mathcal{H}_{1/2,0}^{\Lambda(1600)}$	5.0	0.1	0.1	0.0	0.0	0.0
$\mathrm{Im}\mathcal{H}_{1/2,0}^{\Lambda(1600)}$	3.7	0.1	0.1	0.0	0.1	0.0
$\mathrm{Re}\mathcal{H}_{-1/2,0}^{\Lambda(1600)}$	8.7	0.1	0.0	0.0	0.0	0.1
$\mathrm{Im}\mathcal{H}_{-1/2,0}^{\Lambda(1600)}$	2.0	0.2	0.0	0.1	0.2	0.0
$\mathrm{Re}\mathcal{H}_{1/2,0}^{\Lambda(1670)}$	0.35	0.01	0.00	0.00	0.01	0.00
$\mathrm{Im}\mathcal{H}_{1/2,0}^{\Lambda(1670)}$	0.22	0.02	0.01	0.00	0.02	0.00
$\mathrm{Re}\mathcal{H}_{-1/2,0}^{\Lambda(1670)}$	0.46	0.02	0.01	0.01	0.02	0.00
$\mathrm{Im}\mathcal{H}_{-1/2,0}^{\Lambda(1670)}$	1.2	0.0	0.0	0.0	0.0	0.0
$\mathrm{Re}\mathcal{H}_{1/2,0}^{\Lambda(1690)}$	0.23	0.02	0.01	0.01	0.01	0.00
$\mathrm{Im}\mathcal{H}_{1/2,0}^{\Lambda(1690)}$	0.44	0.02	0.02	0.00	0.01	0.00
$\mathrm{Re}\mathcal{H}_{-1/2,0}^{\Lambda(1690)}$	2.4	0.0	0.0	0.0	0.0	0.0
$\mathrm{Im}\mathcal{H}_{-1/2,0}^{\Lambda(1690)}$	0.60	0.06	0.04	0.03	0.03	0.00
$\mathrm{Re}\mathcal{H}_{1/2,0}^{\Lambda(2000)}$	11	0	0	0	0	0
$\mathrm{Im}\mathcal{H}_{1/2,0}^{\Lambda(2000)}$	7.7	0.2	0.2	0.0	0.1	0.0
$\mathrm{Re}\mathcal{H}_{-1/2,0}^{\Lambda(2000)}$	3.4	0.2	0.1	0.0	0.1	0.0
$\mathrm{Im}\mathcal{H}_{-1/2,0}^{\Lambda(2000)}$	3.7	0.1	0.1	0.0	0.0	0.0
$m^{\Lambda(2000)}$ [MeV]	21	1	1	0	0	0
$\Gamma^{\Lambda(2000)}$ [MeV]	16	3	3	1	0	0

the momentum of the decay products in the $\Lambda_c^+ \to K^* p$ decay, and the opening of $K\eta$, $K\eta'$ decay channels, are neglected in the default fit.

The $\Lambda(1405)$ resonance, having its pole mass below the pK^- threshold, is parametrized by a Flatté line shape [61] describing the opening of the pK decay channel in addition to the $\Sigma\pi$ decay. It is composed of a Breit-Wigner line shape, Eq. (D1), with a total width being the sum of the widths associated to the two decay channels,

$$\Gamma(m) = \Gamma_{pK}(m) + \Gamma_{\Sigma\pi}(m), \tag{12}$$

which are calculated considering the decay to $\Sigma\pi$ (see Appendix D). Assuming that both channels are

TABLE III. Systematic uncertainty contributions on fit parameters describing the K^* and Δ^{++} contributions. Total* includes all contributions except for the choice of the amplitude model.

Parameter	Model choice	Total*	Background	Kinematics	PID	Fit bias
$\mathrm{Re}\mathcal{H}^{K_0^*(700)}_{1/2,0}$	2.1	0.2	0.2	0.1	0.0	0.0
$\mathrm{Im}\mathcal{H}^{K_0^*(700)}_{1/2,0}$	1.3	0.1	0.0	0.0	0.0	0.0
$\mathrm{Re}\mathcal{H}^{K_0^*(700)}_{-1/2,0}$	0.93	0.09	0.07	0.00	0.05	0.01
$\mathrm{Im}\mathcal{H}^{K_0^*(700)}_{-1/2,0}$	3.2	0.1	0.1	0.0	0.0	0.0
$\gamma^{K_0^*(700)}$ [GeV^{-2}]	0.35	0.04	0.03	0.02	0.00	0.00
$\mathrm{Re}\mathcal{H}^{K^*(892)}_{1/2,0}$			0 (fixed)			
$\mathrm{Im}\mathcal{H}^{K^*(892)}_{1/2,0}$			0 (fixed)			
$\mathrm{Re}\mathcal{H}^{K^*(892)}_{1/2,-1}$	0.85	0.05	0.04	0.01	0.02	0.01
$\mathrm{Im}\mathcal{H}^{K^*(892)}_{1/2,-1}$	0.96	0.02	0.02	0.00	0.00	0.01
$\mathrm{Re}\mathcal{H}^{K^*(892)}_{-1/2,1}$	2.4	0.1	0.0	0.0	0.0	0.0
$\mathrm{Im}\mathcal{H}^{K^*(892)}_{-1/2,1}$	2.7	0.1	0.1	0.0	0.0	0.0
$\mathrm{Re}\mathcal{H}^{K^*(892)}_{-1/2,0}$	1.5	0.1	0.0	0.0	0.1	0.0
$\mathrm{Im}\mathcal{H}^{K^*(892)}_{-1/2,0}$	4.5	0.1	0.1	0.0	0.0	0.0
$\mathrm{Re}\mathcal{H}^{K_0^*(1430)}_{1/2,0}$	2.4	0.3	0.2	0.1	0.1	0.0
$\mathrm{Im}\mathcal{H}^{K_0^*(1430)}_{1/2,0}$	9.7	0.1	0.1	0.0	0.0	0.1
$\mathrm{Re}\mathcal{H}^{K_0^*(1430)}_{-1/2,0}$	5.4	0.4	0.3	0.1	0.2	0.0
$\mathrm{Im}\mathcal{H}^{K_0^*(1430)}_{-1/2,0}$	14	0	0	0	0	0
$\gamma^{K_0^*(1430)}$ [GeV^{-2}]	0.33	0.01	0.00	0.00	0.00	0.00
$\mathrm{Re}\mathcal{H}^{\Delta(1232)^{++}}_{1/2,0}$	5.3	0.2	0.2	0.0	0.0	0.0
$\mathrm{Im}\mathcal{H}^{\Delta(1232)^{++}}_{1/2,0}$	1.4	0.1	0.1	0.0	0.1	0.0
$\mathrm{Re}\mathcal{H}^{\Delta(1232)^{++}}_{-1/2,0}$	12	0	0	0	0	0
$\mathrm{Im}\mathcal{H}^{\Delta(1232)^{++}}_{-1/2,0}$	3.7	0.3	0.3	0.1	0.2	0.0
$\mathrm{Re}\mathcal{H}^{\Delta(1600)^{++}}_{1/2,0}$	9.8	0.2	0.2	0.1	0.1	0.1
$\mathrm{Im}\mathcal{H}^{\Delta(1600)^{++}}_{1/2,0}$	1.4	0.2	0.0	0.1	0.2	0.0
$\mathrm{Re}\mathcal{H}^{\Delta(1600)^{++}}_{-1/2,0}$	7.2	0.2	0.2	0.1	0.1	0.0
$\mathrm{Im}\mathcal{H}^{\Delta(1600)^{++}}_{-1/2,0}$	2.1	0.1	0.0	0.0	0.1	0.0
$\mathrm{Re}\mathcal{H}^{\Delta(1700)^{++}}_{1/2,0}$	7.2	0.3	0.3	0.1	0.0	0.1
$\mathrm{Im}\mathcal{H}^{\Delta(1700)^{++}}_{1/2,0}$	5.2	0.2	0.1	0.1	0.1	0.0
$\mathrm{Re}\mathcal{H}^{\Delta(1700)^{++}}_{-1/2,0}$	13	0	0	0	0	0
$\mathrm{Im}\mathcal{H}^{\Delta(1700)^{++}}_{-1/2,0}$	6.0	0.3	0.2	0.1	0.1	0.0

dynamically equally likely and differ only by the phase-space factors, the Breit-Wigner width Γ_0 is set to the total width of the $\Lambda(1405)$ resonance in both terms.

V. UNCERTAINTIES AND CONSISTENCY CHECKS

Statistical and systematic uncertainties are computed for amplitude model parameters, polarization components, fit fractions, decay asymmetry parameters and sensitivity to the polarization. Statistical uncertainties are obtained fitting the default model to 1000 pseudoexperiments sampled with Monte Carlo methods from the same model with parameters fixed to the central values obtained in the real data fit. For each pseudoexperiment the simulation sample used to compute the model normalization is also generated to reproduce finite size effects. Pseudoexperiments and simulation samples are generated with the same size as for the amplitude fit. Statistical uncertainties for each parameter are determined as the standard deviation of the distribution of the results from the pseudoexperiments. Statistical uncertainties are reported along with the final results in Sec. VI; they are found to be larger than the Hessian uncertainties computed in the fit but significantly smaller than the main source of systematic uncertainty.

Different sources of systematic uncertainties are considered. These are grouped into contributions coming from the model choice, the background determination, the kinematics of the decay, the PID, and the fit bias. Since the model choice is the largest contribution for most of the measured quantities, it is quoted separately from the other systematic contributions, which are combined in the final results.

The systematic uncertainty associated to the amplitude model choice is estimated by determining the measured parameters employing alternative models, with fit quality similar to the default fit. They include: leaving as free fit parameters the Breit-Wigner parameters of resonances having fixed mass and width in the default model; addition of the $\Lambda(1800)$, $\Lambda(1810)$ and $\Delta(1620)^{++}$ states; use of a relativistic Breit-Wigner function for describing the $K_0^*(700)$ and $K_0^*(1430)$ line shapes; varying the Λ_c^+ radius in the line shape (see Appendix D); and using spin-orbit instead of helicity couplings. Each modification to the default amplitude model described in Table I is considered separately. The maximum absolute variation among the alternative models, with respect to the default model parameters, is assigned as systematic uncertainty.

The uncertainty associated to the background description includes the uncertainty on the background fraction f_b, estimated using an alternative model for the $m(pK^-\pi^+)$ mass shape, and that on the Legendre polynomial

TABLE IV. Systematic uncertainty contributions on polarization components in percentage. Total* includes all contributions except for the choice of the amplitude model.

Parameter	Model choice	Total*	Background	Kinematics	PID	Fit bias
P_x (lab)	0.98	0.21	0.10	0.17	0.05	0.05
P_y (lab)	0.16	0.07	0.03	0.04	0.05	0.00
P_z (lab)	0.3	1.1	0.0	1.0	0.2	0.0
P_x $(\tilde{B})$	0.36	0.15	0.02	0.15	0.01	0.05
P_y $(\tilde{B})$	0.087	0.081	0.019	0.057	0.054	0.001
P_z $(\tilde{B})$	1.1	0.1	0.1	0.1	0.1	0.0

TABLE V. Systematic uncertainty contributions on fit fractions. Total* includes all contributions except for the choice of the amplitude model.

Resonance FF	Model choice	Total*	Background	Kinematics	PID	Fit bias
$\Lambda(1405)$	0.030	0.002	0.002	0.001	0.000	0.000
$\Lambda(1520)$	0.0023	0.0003	0.0000	0.0002	0.0001	0.0002
$\Lambda(1600)$	0.019	0.001	0.001	0.000	0.000	0.000
$\Lambda(1670)$	0.0032	0.0001	0.0001	0.0000	0.0001	0.0000
$\Lambda(1690)$	0.0034	0.0001	0.0001	0.0001	0.0001	0.0000
$\Lambda(2000)$	0.0093	0.0023	0.0020	0.0010	0.0004	0.0001
$\Delta(1232)^{++}$	0.0076	0.0016	0.0014	0.0003	0.0006	0.0002
$\Delta(1600)^{++}$	0.015	0.001	0.000	0.000	0.000	0.000
$\Delta(1700)^{++}$	0.0094	0.0007	0.0005	0.0004	0.0001	0.0001
$K_0^*(700)$	0.0092	0.0018	0.0018	0.0005	0.0002	0.0001
$K^*(892)$	0.0064	0.0004	0.0000	0.0003	0.0002	0.0002
$K_0^*(1430)$	0.027	0.001	0.001	0.001	0.000	0.000

TABLE VI. Systematic uncertainties on $\sqrt{3}S$ and decay asymmetry parameters. Total* includes all contributions except for the choice of the amplitude model.

α	Model choice	Total*	Background	Kinematics	PID	Fit bias
Model $\sqrt{3}S$	0.010	0.007	0.002	0.002	0.001	0.007
$K^*(892)$ $\sqrt{3}S$	0.023	0.003	0.001	0.000	0.002	0.002
$\Lambda(1405)$	0.28	0.01	0.01	0.00	0.00	0.00
$\Lambda(1520)$	0.084	0.005	0.000	0.001	0.003	0.004
$\Lambda(1600)$	0.50	0.03	0.02	0.01	0.00	0.01
$\Lambda(1670)$	0.073	0.006	0.001	0.002	0.004	0.003
$\Lambda(1690)$	0.027	0.006	0.004	0.002	0.002	0.004
$\Lambda(2000)$	0.19	0.01	0.01	0.00	0.00	0.00
$\Delta(1232)^{++}$	0.036	0.004	0.003	0.000	0.002	0.000
$\Delta(1600)^{++}$	0.17	0.01	0.01	0.00	0.01	0.00
$\Delta(1700)^{++}$	0.075	0.011	0.007	0.005	0.003	0.006
$K_0^*(700)$	0.24	0.23	0.02	0.01	0.00	0.23
$K_0^*(1430)$	0.14	0.01	0.01	0.00	0.01	0.00

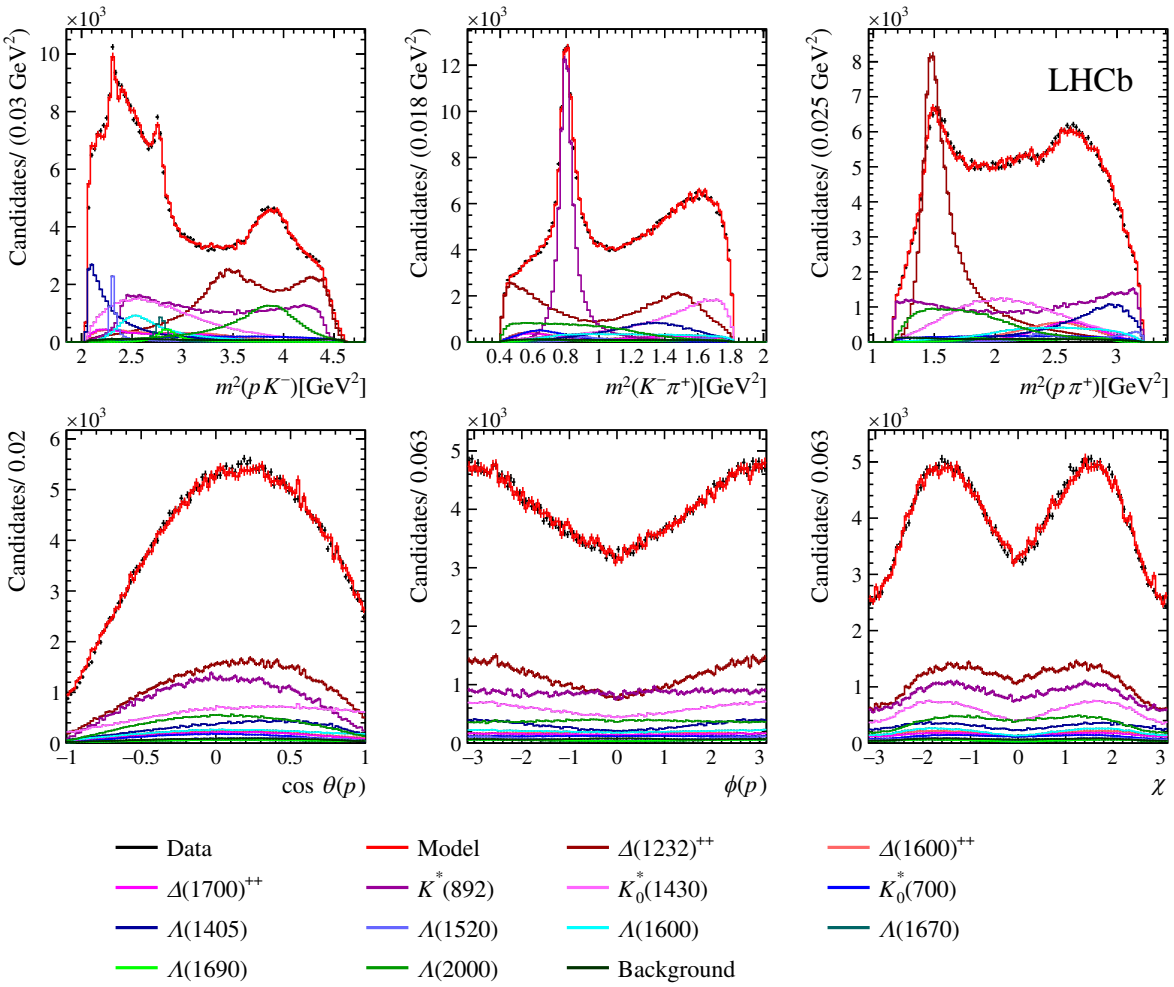

FIG. 3. Distributions for selected candidates together with amplitude fit projections in the *lab* system for (top row) invariant mass squared projections; (bottom row) decay orientation angle projections.

parametrization, estimated using an alternative parametrization determined from the upper mass sideband only. The uncertainty on f_b is at the 10^{-3} level. The uncertainties related to the corrections applied to the simulation are estimated varying the calibration samples employed and the functional form of the corrections, separately for the baryon kinematics and particle identification. A possible bias in the determination of fit parameters is considered by assigning the mean deviation of 1000 pseudoexperiments from the default result as systematic uncertainty. Systematic uncertainties for contributions from fit parameters, polarization components, fit fractions, and decay asymmetries are reported in Tables II–VI.

The stability of the default amplitude model is checked by repeating the fit splitting the dataset for different data-taking magnet polarities, Λ_c^+ charge, Λ_c^+ transverse momentum, Λ_c^+ lifetime, and polarization systems. All the amplitude models obtained are compatible within uncertainties with the default one. Detector resolution effects on invariant masses are found to be 1 order of magnitude smaller than the width of the two narrowest structures, $\Lambda(1520)$ and $\Lambda(1670)$, and are not considered.

VI. RESULTS

The comparison between $\Lambda_c^+ \to pK^-\pi^+$ data and default amplitude fit projections is displayed in Figs. 3 and 4 for Λ_c^+ polarization in the laboratory or approximate B systems, respectively. The amplitude model distributions are obtained from the $\Lambda_c^+ \to pK^-\pi^+$ simulation sample which reproduces detector efficiency effects. The fit qualities are good given the large number of events.

The polarization components in the laboratory and approximate B systems are reported in Table VII. This analysis demonstrates the possibility of a precision measurement of the full Λ_c^+ polarization vector, with absolute uncertainties of order 1% on each component. A large polarization is measured in both Λ_c^+ helicity frames considered. In the one reached from the laboratory it has a modulus $P \approx 65\%$, with a dominating positive transverse component $P_x \approx 60\%$ and a smaller negative longitudinal

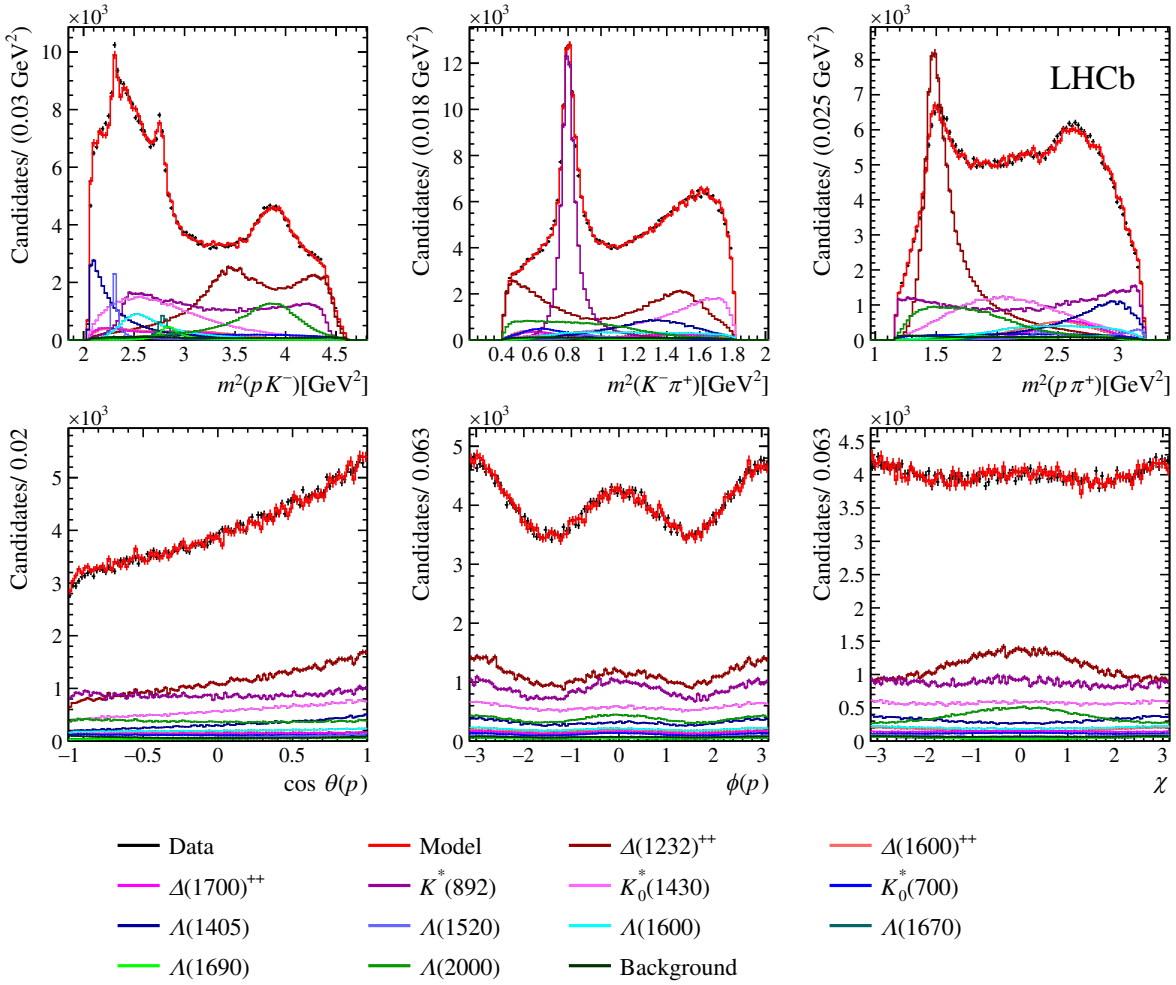

FIG. 4. Distributions for selected candidates together with amplitude fit projections in the $\tilde{B}$ system for (top row) invariant mass squared projections; (bottom row) decay orientation angle projections.

TABLE VII. Measured polarization components. The first uncertainty is statistical, the second is the amplitude model choice systematic contribution and the third is the combination of the other systematic uncertainties.

Component	Value (%)
P_x (lab)	$60.32 \pm 0.68 \pm 0.98 \pm 0.21$
P_y (lab)	$-0.41 \pm 0.61 \pm 0.16 \pm 0.07$
P_z (lab)	$-24.7 \pm 0.6 \pm 0.3 \pm 1.1$
P_x $(\tilde{B})$	$21.65 \pm 0.68 \pm 0.36 \pm 0.15$
P_y $(\tilde{B})$	$1.08 \pm 0.61 \pm 0.09 \pm 0.08$
P_z $(\tilde{B})$	$-66.5 \pm 0.6 \pm 1.1 \pm 0.1$

component $P_z \approx -25\%$. In the system reached from the approximate beauty hadron rest frame it has a modulus $P \approx 70\%$, with a dominating negative longitudinal component $P_z \approx -66\%$ and a smaller positive transverse component $P_x \approx 22\%$. The latter polarization components follow the theoretical predictions [6,9,10,15,18,26,27]. A precise comparison of the measured Λ_c^+ polarization values with theoretical predictions is beyond the scope of the present analysis. This would require an exclusive selection of $\Lambda_b^0 \to \Lambda_c^+\mu^-\nu$ decays from other contributions, like those from excited charm resonances $\Lambda_b^0 \to \Lambda_c^{*+}(\to\Lambda_c^+\pi^+\pi^-)\mu^-\nu$, and an understanding of the effect of partial semileptonic decay

TABLE VIII. Default amplitude model measured fit parameters describing the Λ contributions.

Parameter	Central value	Statistical uncertainty	Model uncertainty	Systematic uncertainty
$\mathrm{Re}\mathcal{H}^{\Lambda(1405)}_{1/2,0}$	−4.6	0.5	3.3	0.1
$\mathrm{Im}\mathcal{H}^{\Lambda(1405)}_{1/2,0}$	3.2	0.5	3.2	0.1
$\mathrm{Re}\mathcal{H}^{\Lambda(1405)}_{-1/2,0}$	10	1	12	0
$\mathrm{Im}\mathcal{H}^{\Lambda(1405)}_{-1/2,0}$	2.8	1.1	3.7	0.3
$\mathrm{Re}\mathcal{H}^{\Lambda(1520)}_{1/2,0}$	0.29	0.05	0.12	0.01
$\mathrm{Im}\mathcal{H}^{\Lambda(1520)}_{1/2,0}$	0.04	0.05	0.12	0.02
$\mathrm{Re}\mathcal{H}^{\Lambda(1520)}_{-1/2,0}$	−0.16	0.14	0.69	0.03
$\mathrm{Im}\mathcal{H}^{\Lambda(1520)}_{-1/2,0}$	1.5	0.1	1.3	0.0
$m^{\Lambda(1520)}$ [MeV]	1518.47	0.36	0.65	0.03
$\Gamma^{\Lambda(1520)}$ [MeV]	15.2	0.8	1.3	0.1
$\mathrm{Re}\mathcal{H}^{\Lambda(1600)}_{1/2,0}$	4.8	0.5	5.0	0.1
$\mathrm{Im}\mathcal{H}^{\Lambda(1600)}_{1/2,0}$	3.1	0.5	3.7	0.1
$\mathrm{Re}\mathcal{H}^{\Lambda(1600)}_{-1/2,0}$	−7.0	0.5	8.7	0.1
$\mathrm{Im}\mathcal{H}^{\Lambda(1600)}_{-1/2,0}$	0.8	0.6	2.0	0.2
$\mathrm{Re}\mathcal{H}^{\Lambda(1670)}_{1/2,0}$	−0.34	0.05	0.35	0.01
$\mathrm{Im}\mathcal{H}^{\Lambda(1670)}_{1/2,0}$	−0.14	0.05	0.22	0.02
$\mathrm{Re}\mathcal{H}^{\Lambda(1670)}_{-1/2,0}$	−0.57	0.10	0.46	0.02
$\mathrm{Im}\mathcal{H}^{\Lambda(1670)}_{-1/2,0}$	1.0	0.1	1.2	0.0
$\mathrm{Re}\mathcal{H}^{\Lambda(1690)}_{1/2,0}$	−0.39	0.10	0.23	0.02
$\mathrm{Im}\mathcal{H}^{\Lambda(1690)}_{1/2,0}$	−0.11	0.09	0.44	0.02
$\mathrm{Re}\mathcal{H}^{\Lambda(1690)}_{-1/2,0}$	−2.7	0.2	2.4	0.0
$\mathrm{Im}\mathcal{H}^{\Lambda(1690)}_{-1/2,0}$	−0.35	0.23	0.60	0.06
$\mathrm{Re}\mathcal{H}^{\Lambda(2000)}_{1/2,0}$	−8	1	11	0
$\mathrm{Im}\mathcal{H}^{\Lambda(2000)}_{1/2,0}$	−7.6	0.8	7.7	0.2
$\mathrm{Re}\mathcal{H}^{\Lambda(2000)}_{-1/2,0}$	−4.3	0.5	3.4	0.2
$\mathrm{Im}\mathcal{H}^{\Lambda(2000)}_{-1/2,0}$	−3.8	0.4	3.7	0.1
$m^{\Lambda(2000)}$ [MeV]	1988	2	21	1
$\Gamma^{\Lambda(2000)}$ [MeV]	179	4	16	3

reconstruction on the polarization components obtained from the true beauty hadron rest frame.

The relation between the two measured polarization vectors can be explained in terms of the different orientation in space of the two polarization systems considered, with the rotation from mostly longitudinal to mostly transverse polarization reproduced by a study performed on simulated events. The leading uncertainty for transverse polarization in both systems and longitudinal polarization in the $\tilde{B}$ frame is that associated to the amplitude model choice, while the main uncertainty on longitudinal polarization in laboratory frame is due to baryon kinematic corrections. The normal polarization P_y, sensitive to time-reversal violation effects and final-state interactions as explained in Appendix A, is compatible with zero at the 1% level, for both polarization systems considered. The dominant uncertainty on P_y is statistical. The reduced impact of systematic contributions on P_y is explained by the fact that this component is

TABLE IX. Default amplitude model measured fit parameters describing the K^* and Δ^{++} contributions.

Parameter	Central value	Statistical uncertainty	Model uncertainty	Systematic uncertainty
$\mathrm{Re}\mathcal{H}^{K_0^*(700)}_{1/2,0}$	−2.7	0.2	2.1	0.2
$\mathrm{Im}\mathcal{H}^{K_0^*(700)}_{1/2,0}$	0.0	0.3	1.3	0.1
$\mathrm{Re}\mathcal{H}^{K_0^*(700)}_{-1/2,0}$	0.07	0.23	0.93	0.09
$\mathrm{Im}\mathcal{H}^{K_0^*(700)}_{-1/2,0}$	2.5	0.2	3.2	0.1
$\gamma^{K_0^*(700)}$ [GeV^{-2}]	0.94	0.07	0.35	0.04
$\mathrm{Re}\mathcal{H}^{K^*(892)}_{1/2,0}$	1 (fixed)			
$\mathrm{Im}\mathcal{H}^{K^*(892)}_{1/2,0}$	0 (fixed)			
$\mathrm{Re}\mathcal{H}^{K^*(892)}_{1/2,-1}$	1.19	0.13	0.85	0.05
$\mathrm{Im}\mathcal{H}^{K^*(892)}_{1/2,-1}$	−1.03	0.12	0.96	0.02
$\mathrm{Re}\mathcal{H}^{K^*(892)}_{-1/2,1}$	−3.1	0.4	2.4	0.1
$\mathrm{Im}\mathcal{H}^{K^*(892)}_{-1/2,1}$	−3.3	0.3	2.7	0.1
$\mathrm{Re}\mathcal{H}^{K^*(892)}_{-1/2,0}$	−0.7	0.3	1.5	0.1
$\mathrm{Im}\mathcal{H}^{K^*(892)}_{-1/2,0}$	−4.2	0.3	4.5	0.1
$\mathrm{Re}\mathcal{H}^{K_0^*(1430)}_{1/2,0}$	0.2	0.8	2.4	0.3
$\mathrm{Im}\mathcal{H}^{K_0^*(1430)}_{1/2,0}$	8.7	0.7	9.7	0.1
$\mathrm{Re}\mathcal{H}^{K_0^*(1430)}_{-1/2,0}$	−6.7	1.0	5.4	0.4
$\mathrm{Im}\mathcal{H}^{K_0^*(1430)}_{-1/2,0}$	10	1	14	0
$\gamma^{K_0^*(1430)}$ [GeV^{-2}]	0.02	0.02	0.33	0.01
$\mathrm{Re}\mathcal{H}^{\Delta(1232)^{++}}_{1/2,0}$	−6.8	0.5	5.3	0.2
$\mathrm{Im}\mathcal{H}^{\Delta(1232)^{++}}_{1/2,0}$	3.1	0.6	1.4	0.1
$\mathrm{Re}\mathcal{H}^{\Delta(1232)^{++}}_{-1/2,0}$	−13	1	12	0
$\mathrm{Im}\mathcal{H}^{\Delta(1232)^{++}}_{-1/2,0}$	4.5	1.1	3.7	0.3
$\mathrm{Re}\mathcal{H}^{\Delta(1600)^{++}}_{1/2,0}$	11.4	0.9	9.8	0.2
$\mathrm{Im}\mathcal{H}^{\Delta(1600)^{++}}_{1/2,0}$	−3.1	1.0	1.4	0.2
$\mathrm{Re}\mathcal{H}^{\Delta(1600)^{++}}_{-1/2,0}$	6.7	0.7	7.2	0.2
$\mathrm{Im}\mathcal{H}^{\Delta(1600)^{++}}_{-1/2,0}$	−1.0	0.7	2.1	0.1
$\mathrm{Re}\mathcal{H}^{\Delta(1700)^{++}}_{1/2,0}$	10.4	0.9	7.2	0.3
$\mathrm{Im}\mathcal{H}^{\Delta(1700)^{++}}_{1/2,0}$	1.4	0.9	5.2	0.2
$\mathrm{Re}\mathcal{H}^{\Delta(1700)^{++}}_{-1/2,0}$	13	1	13	0
$\mathrm{Im}\mathcal{H}^{\Delta(1700)^{++}}_{-1/2,0}$	2.1	1.1	6.0	0.3

compatible with zero: indeed the presence of a polarization component is model independent (can be seen directly from decay orientation angle distribution), while the determination of the polarization magnitude depends on the resonance interference pattern described by the amplitude model [1].

The measured parameters of the default amplitude model, for Λ_c^+ polarization measured in the *lab* system, are reported in Tables VIII and IX, fit fractions for each resonant contribution in Table X, $\sqrt{3}S$ and two-body decay asymmetry parameters in Table XI. As studied in Ref. [1], the $\Lambda_c^+ \to pK^-\pi^+$ amplitude analysis is sensitive to all the parameters describing the $\Lambda_c^+ \to pK^-\pi^+$ amplitude model, thanks to the significant Λ_c^+ polarization and interference effects among different decay chains. The leading uncertainty comes from the amplitude model choice for all parameters.

A significant contribution from a resonant state in the $m(pK^-) \approx 2$ GeV region, where clear resonances have not previously been reported by Ref. [25], has been established. This contribution is well described as a single $J^P = 1/2^-$ state, with Breit-Wigner parameters $m = 1988 \pm 2 \pm 21$ and $\Gamma = 179 \pm 4 \pm 16$ MeV, where the first uncertainty is statistical the second combines all the systematic sources. The closest resonance reported by Ref. [25] is the $\Lambda(2000)$: the measured values are fairly compatible with those quoted by Ref. [62], $m = 2020 \pm 16$ and $\Gamma = 255 \pm 63$ MeV, and Ref. [63], $m = 2030 \pm 30$ and $\Gamma = 125 \pm 25$ MeV. This structure can be therefore interpreted as a $\Lambda(2000)$ state contribution.

The largest contributions to the amplitude model, measured from fit fractions, come from the $\Delta(1232)^{++}$, $K^*(892)$ and $K_0^*(1430)$ resonances. Among the Λ resonances the largest contributions are from the $\Lambda(1405)$ and $\Lambda(2000)$ states. The $\Lambda(1520)$ parameters are compatible with those reported by Ref. [25].

TABLE X. Fit fractions of the resonant contributions included in the default amplitude model. The first uncertainty is statistical, the second is amplitude model choice systematic contribution, the third is the combination of the other systematic uncertainties.

Resonance	Fit fraction (%)	Statistical uncertainty	Model uncertainty	Systematic uncertainty
$\Lambda(1405)$	7.7	0.2	3.0	0.2
$\Lambda(1520)$	1.86	0.09	0.23	0.03
$\Lambda(1600)$	5.2	0.2	1.9	0.1
$\Lambda(1670)$	1.18	0.06	0.32	0.01
$\Lambda(1690)$	1.19	0.09	0.34	0.01
$\Lambda(2000)$	9.58	0.27	0.93	0.23
$\Delta(1232)^{++}$	28.60	0.29	0.76	0.16
$\Delta(1600)^{++}$	4.5	0.3	1.5	0.1
$\Delta(1700)^{++}$	3.90	0.20	0.94	0.07
$K_0^*(700)$	3.02	0.16	0.92	0.18
$K^*(892)$	22.14	0.23	0.64	0.04
$K_0^*(1430)$	14.7	0.6	2.7	0.1

TABLE XI. Sensitivity to polarization $\sqrt{3}S$ of the default amplitude model and decay asymmetry α parameters of single resonant contributions. The first uncertainty is statistical, the second is the amplitude model choice systematic contribution, the third is the combination of the other systematic uncertainties.

Resonance	α	Statistical uncertainty	Model uncertainty	Systematic uncertainty
Model $\sqrt{3}S$	0.662	0.005	0.010	0.007
$K^*(892)$ $\sqrt{3}S$	0.873	0.010	0.023	0.003
$\Lambda(1405)$	−0.58	0.05	0.28	0.01
$\Lambda(1520)$	−0.925	0.025	0.084	0.005
$\Lambda(1600)$	−0.20	0.06	0.50	0.03
$\Lambda(1670)$	−0.817	0.042	0.073	0.006
$\Lambda(1690)$	−0.958	0.020	0.027	0.006
$\Lambda(2000)$	−0.57	0.03	0.19	0.01
$\Delta(1232)^{++}$	−0.548	0.014	0.036	0.004
$\Delta(1600)^{++}$	−0.50	0.05	0.17	0.01
$\Delta(1700)^{++}$	−0.216	0.036	0.075	0.011
$K_0^*(700)$	−0.06	0.66	0.24	0.23
$K_0^*(1430)$	−0.34	0.03	0.14	0.01

A large sensitivity of the $\Lambda_c^+ \to pK^-\pi^+$ decay to the polarization is measured, $\sqrt{3}S = 0.662 \pm 0.005 \pm 0.015$, which is also an observation of parity violation in the decay. The large sensitivity, combined with the large value of the branching fraction, makes the $\Lambda_c^+ \to pK^-\pi^+$ decay the best probe for Λ_c^+ polarization and spin precession measurements, providing the smallest uncertainties. Many two-body decay asymmetry parameters are significantly different from zero, indicating parity violation. In particular, the α parameter associated to the $3/2^+$ $\Delta(1232)^{++}$ contribution is nonzero, in contrast with the prediction of Ref. [2].

VII. SUMMARY

A full amplitude analysis of $\Lambda_c^+ \to pK^-\pi^+$ decays with measurement of the Λ_c^+ polarization vector in semileptonic beauty hadron decays is presented. A sample of 400 000 candidates is selected from proton-proton collisions recorded by the LHCb detector at a center-of-mass energy of 13 TeV, featuring a very small residual background contribution. The amplitude model is written in the helicity formalism with a general method to deal with the matching of final particle spin states in different decay chains and includes a generic Λ_c^+ polarization vector. A maximum-likelihood fit is performed to determine the amplitude model parameters. All the parameters of the amplitude model and the baryon polarization have been measured; fit fractions and decay asymmetry parameters for each two-body resonant contribution are also reported together with the effective three-body decay asymmetry parameter of the $\Lambda_c^+ \to pK^-\pi^+$ decay. The most important resonances contributing to the $\Lambda_c^+ \to pK^-\pi^+$ decay are from $\Delta(1232)^{++}$, $K^*(892)$ and spin-zero K^* states. A significant enhancement in the $m^2_{pK^-}$ spectrum, in a region where no clear Λ resonances have been reported in Ref. [25], is well described by a spin $1/2^-$ state, identified as a $\Lambda(2000)$ resonance. Its mass and width parameters are determined to be $1988 \pm 2 \pm 21$ and $179 \pm 4 \pm 16$ MeV, respectively. A large Λ_c^+ polarization is found, of order 65%–70%, measured with absolute uncertainties of order 1%. The normal polarization, sensitive to time-reversal violation effects and final-state interactions, is compatible with zero. A large sensitivity to the polarization is measured, showing the $\Lambda_c^+ \to pK^-\pi^+$ decay to be the best probe for Λ_c^+ polarization. The amplitude model obtained provides a complete description of the $\Lambda_c^+ \to pK^-\pi^+$ decay, with applications ranging from new physics searches to low-energy QCD. Such applications include an increased sensitivity to angular analyses of semileptonic baryon decays, and the most precise measurements of the Λ_c^+ polarization and electromagnetic dipole moments via spin precession.

ACKNOWLEDGMENTS

We express our gratitude to our colleagues in the CERN accelerator departments for the excellent performance of the LHC. We thank the technical and administrative staff at the LHCb institutes. We acknowledge support from CERN and from the national agencies: CAPES, CNPq, FAPERJ and FINEP (Brazil); MOST and NSFC (China); CNRS/IN2P3 (France); BMBF, DFG and MPG (Germany); INFN (Italy); NWO (Netherlands); MNiSW and NCN (Poland); MEN/IFA (Romania); MICINN (Spain); SNSF and SER (Switzerland); NASU (Ukraine); STFC (United Kingdom); and DOE NP and NSF (USA). We acknowledge the computing resources that are provided by CERN, IN2P3 (France), KIT and DESY (Germany), INFN (Italy), SURF (Netherlands), PIC (Spain), GridPP (United Kingdom), CSCS (Switzerland), IFIN-HH (Romania), CBPF (Brazil), Polish WLCG (Poland) and NERSC (USA). We are indebted to the communities behind the multiple open-source software packages on which we depend. Individual groups or members have received support from ARC and ARDC (Australia); Minciencias (Colombia); AvH Foundation (Germany); EPLANET, Marie Skłodowska-Curie Actions and ERC (European Union); A*MIDEX, ANR, IPhU and Labex P2IO, and Région Auvergne-Rhône-Alpes (France); Key Research Program of Frontier Sciences of CAS, CAS PIFI, CAS CCEPP, Fundamental Research Funds for the Central Universities, and Sci. & Tech. Program of Guangzhou (China); GVA, XuntaGal, GENCAT and Prog. Atracción Talento, CM (Spain); SRC (Sweden); the Leverhulme Trust, the Royal Society and UKRI (United Kingdom).

APPENDIX A: AMPLITUDE MODEL

The helicity formalism allows the association of a decay amplitude to a two-body decay, dependent on the spin projection of the decaying particle and the helicities of the final-state particles. The amplitude is obtained establishing a relation between two sets of two-particle states: plane-wave helicity states, describing propagating particles with well defined momentum; and spherical-wave helicity states, describing states of definite total angular momentum. In Ref. [38] the plane-wave two-particle state is defined by the product of a pair of helicity and opposite-helicity states,

$$|p, \theta_1, \phi_1, \lambda_1, \bar{\lambda}_2\rangle \equiv |\boldsymbol{p}_1, s_1, \lambda_1\rangle \otimes |\boldsymbol{p}_2, s_2, \bar{\lambda}_2\rangle, \qquad \text{(A1)}$$

instead of the product of helicity states for both final particles as in Ref. [55]. Helicity (opposite-helicity) states are those in which the spin is quantized along (opposite to) the momentum direction. Helicity values are indicated with λ ($\bar{\lambda}$); while p, θ_1 and ϕ_1 are the spherical coordinates of the momentum $\boldsymbol{p}_1$ of particle 1 in the two-particle center-of-mass frame,

$$
\begin{aligned}
p &= |\boldsymbol{p}_1|,\\
\theta_1 &= \arccos(\hat{\boldsymbol{z}}\cdot\hat{\boldsymbol{p}}_1),\\
\phi_1 &= \arctan(\hat{\boldsymbol{y}}\cdot\hat{\boldsymbol{p}}_1, \hat{\boldsymbol{x}}\cdot\hat{\boldsymbol{p}}_1),
\end{aligned}
\tag{A2}
$$

where the coordinate axes are those representing the total angular momentum components. The function $\arctan(y,x) \in [-\pi,\pi]$ computes the signed angle between the x axis and the vector having components (x,y). The relation expressing plane-wave states in terms of spherical-wave states is

$$
\begin{aligned}
|p,\theta_1,\phi_1,\lambda_1,\bar{\lambda}_2\rangle = \sum_{J,M} \sqrt{\frac{2J+1}{4\pi}} D^J_{M,\lambda_1+\bar{\lambda}_2}(\phi_1,\theta_1,0)\\
\times |p,J,M,\lambda_1,\bar{\lambda}_2\rangle,
\end{aligned}
\tag{A3}
$$

where $D^J_{M,\lambda_1+\bar{\lambda}_2}(\phi_1,\theta_1,0)$ is the Wigner D-matrix representing the Euler rotation from the total momentum spin system to the particle 1 helicity system. A basic introduction to Euler rotations and their representation on spin states is given in Appendix B.

With the present definition of plane-wave states, both final-state particle spin states are defined by the same rotation $R(\phi_1,\theta_1,0)$ (details are given in Ref. [38]), without the need to invert the particle 2 helicity states as in Ref. [55]. This choice of the two-particle state eases the handling of phase differences and the matching of proton spin states, addressed later in the construction of the $\Lambda_c^+ \to pK^-\pi^+$ amplitude model.

The amplitude associated to a two-body decay $A \to 12$, with $\hat{T}$ the relevant transition operator, is obtained by introducing the A particle spin states $|s_A, m_A\rangle$,

$$
\begin{aligned}
\mathcal{A}_{m_A,\lambda_1,\bar{\lambda}_2}(\theta_1,\phi_1) &\equiv \langle p,\theta_1,\phi_1,\lambda_1,\bar{\lambda}_2|\hat{T}|s_A,m_A\rangle\\
&= \mathcal{H}_{\lambda_1,\bar{\lambda}_2} D^{*s_A}_{m_A,\lambda_1+\bar{\lambda}_2}(\phi_1,\theta_1,0)\mathcal{R}(m_{12}^2),
\end{aligned}
\tag{A4}
$$

in which the Wigner D-matrix contains the dependence of the decay amplitude on the helicity angles. The decay dynamics is described by complex numbers called helicity couplings,

$$
\mathcal{H}_{\lambda_1,\bar{\lambda}_2} \equiv \langle s_A, m_A, \lambda_1, \bar{\lambda}_2|\hat{T}|s_A,m_A\rangle,
\tag{A5}
$$

and a (line shape) function $\mathcal{R}(m_{12}^2)$, modeling the dependence on the decaying A particle invariant mass, in case it has a non-negligible width. Helicity couplings cannot depend on s_A, m_A by rotational invariance. The helicity values allowed by angular momentum conservation are

$$
|\lambda_1| \le s_1, \qquad |\bar{\lambda}_2| \le s_2, \qquad |\lambda_1 + \bar{\lambda}_2| \le s_A.
\tag{A6}
$$

If the decay respects parity symmetry, the helicity couplings for opposite helicities are constrained by the relation

$$
\mathcal{H}_{\lambda_1,\bar{\lambda}_2} \equiv \eta_A\eta_1\eta_2(-1)^{s_1+s_2-s_A}\mathcal{H}_{-\lambda_1,-\bar{\lambda}_2},
\tag{A7}
$$

where η are the parity eigenvalues of the particle states.

1. Λ_c^+ baryon polarization and decay kinematics

Charm baryons in semileptonic beauty decays are polarized due to the parity-violating nature of the weak interaction. The Λ_c^+ polarization is measured using helicity coordinate systems defined from Λ_c^+ and muon momenta in two reference frames: the laboratory frame (*lab*), precisely determined, and an approximate beauty hadron rest frame ($\tilde{B}$). The latter is obtained assuming the proper velocity along the beam axis, $\gamma\beta_z$, of the reconstructed $\Lambda_c^+\mu^-$ pair is equal to that of the beauty baryon.

The Λ_c^+ momentum defines the longitudinal P_z polarization component, the muon momentum component orthogonal to the Λ_c^+ momentum defines the orthogonal P_x component, with the normal P_y component defined through a right-handed system, as shown in Fig. 5,

$$
\begin{aligned}
P_z &= \boldsymbol{P}\cdot\hat{\boldsymbol{z}}_{\Lambda_c^+} = \boldsymbol{P}\cdot\hat{\boldsymbol{p}}(\Lambda_c^+),\\
P_x &= \boldsymbol{P}\cdot\hat{\boldsymbol{x}}_{\Lambda_c^+} = \boldsymbol{P}\cdot\left[\frac{\boldsymbol{p}(\Lambda_c^+)\times\boldsymbol{p}(\mu^-)}{|\boldsymbol{p}(\Lambda_c^+)\times\boldsymbol{p}(\mu^-)|}\times\hat{\boldsymbol{p}}(\Lambda_c^+)\right],\\
P_y &= \boldsymbol{P}\cdot\hat{\boldsymbol{y}}_{\Lambda_c^+} = \boldsymbol{P}\cdot\frac{\boldsymbol{p}(\Lambda_c^+)\times\boldsymbol{p}(\mu^-)}{|\boldsymbol{p}(\Lambda_c^+)\times\boldsymbol{p}(\mu^-)|}.
\end{aligned}
\tag{A8}
$$

Considering the effect of the time-reversal operation T, longitudinal and transverse components are T-even quantities, while normal polarization is T-odd, implying the latter to be produced only by time-reversal violating effects or final-state interactions between particles produced in the semileptonic decay [64]. Final-state interactions between the Λ_c^+ and μ^- particles can occur due to electromagnetic interactions only, expected to be $\mathcal{O}(1\%)$. The T-odd property of normal polarization does not depend on the reference system used for its definition, as studied with $\Lambda_b^0 \to \Lambda_c^+\mu^-\bar{\nu}_\mu$ simulated decays. It has been checked that a null P_y in the helicity system reached from the true Λ_b^0 rest frame is zero also when rotated to the helicity systems reached from the laboratory or the approximate B systems; the polarization rotation is confined to the zx plane.

The 5 degrees of freedom of a baryon three-body decay can be described by the following quantities: two two-body invariant mass squared ("Dalitz" variables) modeling the decay dynamics and three decay orientation angles describing the decay plane orientation with respect to the baryon polarization system; the latter are important when the baryon polarization is considered. For the $\Lambda_c^+ \to pK^-\pi^+$ decay, $m^2_{pK^-}$ and $m^2_{K^-\pi^+}$ are selected as Dalitz variables. The decay orientation angles are defined to be the Euler angles describing the rotation from the polarization system in Eq. (A8) to a decay plane (DP) reference system constructed as follows: the proton momentum defines

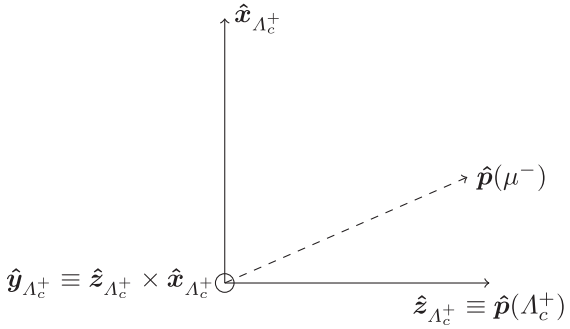

FIG. 5. Definition of the Λ_c^+ polarization system. The $\hat{\boldsymbol{y}}_{\Lambda_c^+}$ axis is orthogonal to the page, towards the reader.

the z axis, while the component of the kaon momentum orthogonal to the proton momentum defines the x axis (see Fig. 5 with $\Lambda_c^+ \leftrightarrow p$, $\mu^- \leftrightarrow K^-$ substitutions),

$$\begin{aligned}\hat{\boldsymbol{z}}_{\mathrm{DP}} &= \hat{\boldsymbol{p}}(p),\\ \hat{\boldsymbol{x}}_{\mathrm{DP}} &= \frac{\boldsymbol{p}(p)\times\boldsymbol{p}(K^-)}{|\boldsymbol{p}(p)\times\boldsymbol{p}(K^-)|}\times\hat{\boldsymbol{p}}(p),\\ \hat{\boldsymbol{y}}_{\mathrm{DP}} &= \hat{\boldsymbol{z}}_{\mathrm{DP}}\times\hat{\boldsymbol{x}}_{\mathrm{DP}},\end{aligned} \tag{A9}$$

where momenta are expressed in the Λ_c^+ rest frame.

With this definition the Euler angles α and β are the azimuthal and polar angles of the proton in the Λ_c^+ polarization system, ϕ_p and θ_p, respectively, and the γ angle is the signed angle named χ formed by the proton and the Λ_c^+ quantization axis $\hat{\boldsymbol{z}}_{\Lambda_c^+}$ and the plane formed by the kaon and the pion. Following Eq. (B3) and the definition in Fig. 6 one has

$$\begin{aligned}\phi_p &= \arctan(\hat{\boldsymbol{p}}(p)\cdot\hat{\boldsymbol{y}}_{\Lambda_c^+}, \hat{\boldsymbol{p}}(p)\cdot\hat{\boldsymbol{x}}_{\Lambda_c^+}),\\ \theta_p &= \arccos(\hat{\boldsymbol{p}}(p)\cdot\hat{\boldsymbol{z}}_{\Lambda_c^+}),\\ \chi &= \arctan\left\{\hat{\boldsymbol{z}}_{\Lambda_c^+}\cdot\frac{\boldsymbol{p}(p)\times\boldsymbol{p}(K^-)}{|\boldsymbol{p}(p)\times\boldsymbol{p}(K^-)|},\right.\\ &\quad\left.-\hat{\boldsymbol{z}}_{\Lambda_c^+}\cdot\left[\frac{\boldsymbol{p}(p)\times\boldsymbol{p}(K^-)}{|\boldsymbol{p}(p)\times\boldsymbol{p}(K^-)|}\times\hat{\boldsymbol{p}}(p)\right]\right\}.\end{aligned} \tag{A10}$$

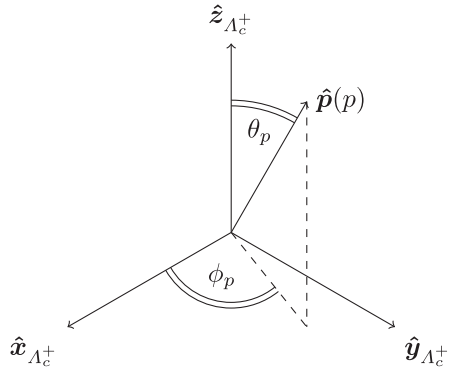

The five phase-space variables are therefore chosen to be

$$\Omega = (m^2_{pK^-}, m^2_{K^-\pi^+}, \cos\theta_p, \phi_p, \chi), \tag{A11}$$

with the phase-space density being uniform over them. Their allowed range is $\cos\theta_p \in [-1,1]$ and $\phi_p, \chi \in [-\pi,\pi]$, while the mass distributions are constrained to a rounded-triangle shape in the $(m^2_{pK^-}, m^2_{K^-\pi^+})$ plane (Dalitz plot, see Fig. 2).

2. Amplitude model for the $\Lambda_c^+ \to pK^-\pi^+$ decay

The amplitude model for the $\Lambda_c^+ \to pK^-\pi^+$ decay is written by decomposing the three-body decay into two sequential two-body decays by introducing intermediate resonant states. Three decay channels are possible: $K^* \to K^-\pi^+$, $\Lambda \to pK^-$ and $\Delta^{++} \to p\pi^+$. Helicity amplitudes are obtained for each channel and summed coherently using the method for matching proton spin states among different decay chains of Ref. [38]. The matching step allows the transformation of proton helicity states, different for each decay channel, to a common definition of proton spin states.

To simplify the amplitude model expression, the invariant mass and decay orientation angle degrees of freedom can be separated applying the Dalitz plot decomposition [65],

$$\begin{aligned}\mathcal{A}_{m_{\Lambda_c^+}, m_p}(\Omega) = &\sum_{\nu_{\Lambda_c^+}} D^{*1/2}_{m_{\Lambda_c^+}, \nu_{\Lambda_c^+}}(\phi_p, \theta_p, \chi)\\ &\times \mathcal{O}_{\nu_{\Lambda_c^+}, m_p}(m^2_{pK^-}, m^2_{K^-\pi^+}),\end{aligned} \tag{A12}$$

in which the Wigner D-matrix describes the rotation of Λ_c^+ spin states from the Λ_c^+ polarization system in Eq. (A8), $|1/2, m_{\Lambda_c^+}\rangle$, to the decay plane system in Eq. (A9), $|1/2, \nu_{\Lambda_c^+}\rangle$. The term $\mathcal{O}_{\nu_{\Lambda_c^+}, m_p}(m^2_{pK^-}, m^2_{K^-\pi^+})$ describes the Λ_c^+ decay amplitudes in terms of Λ_c^+ spin states $|1/2, \nu_{\Lambda_c^+}\rangle$ and proton states defined in the canonical spin system reached from the Λ_c^+ decay plane system, $|1/2, m_p\rangle$. These

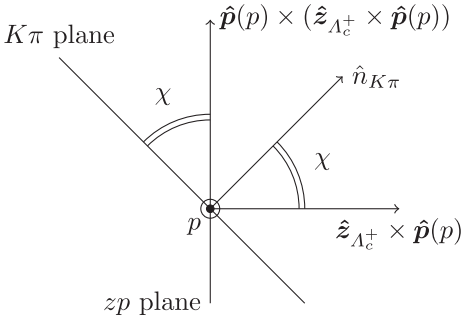

FIG. 6. Definition of the Euler angles describing the rotation from the Λ_c^+ polarization system to the decay plane reference system: (left) proton polar and azimuthal angles and (right) χ angle.

proton states are later employed for the matching of proton spin states among different decay chains. The decomposition allows the definition of helicity and canonical spin states using polar rotations only, around the y axis of the decay plane system. Therefore, the angular part of the decay amplitude simplifies, depending solely on polar helicity angles via reduced Wigner d-matrices.

Considering the $\Lambda_c^+ \to pK^*(\to K^-\pi^+)$ decay chain, the weak $\Lambda_c^+ \to pK^*$ decay amplitude is given by Eq. (A4) applied starting from the decay plane coordinate system,

$$\mathcal{A}^{\Lambda_c^+\to pK^*}_{\nu_{\Lambda_c^+},m_p,\bar{\lambda}_{K^*}} = \mathcal{H}^{\Lambda_c^+\to pK^*}_{m_p,\bar{\lambda}_{K^*}} \delta_{\nu_{\Lambda_c^+},m_p+\bar{\lambda}_{K^*}}, \tag{A13}$$

where spin states are expressed in the DP system, and the amplitude is written in terms of the proton helicity m_p and the K^* opposite helicity $\bar{\lambda}_{K^*}$. The proton helicity states reached from the DP system coincide with the canonical states since in the DP system the proton momentum is already aligned to the quantization axis. Since no rotation of spin states is involved, the D-matrix becomes a constraint on the helicity values $m_p + \bar{\lambda}_{K^*} = \nu_{\Lambda_c^+}$.

For spin-zero K^* resonances the angular momentum conservation relations in Eq. (A6) allow two complex couplings corresponding to $m_p = \pm 1/2$. For higher-spin resonances, four couplings are allowed, corresponding to $\{m_p = 1/2; \bar{\lambda}_{K^*} = 0, -1\}$ and $\{m_p = -1/2; \bar{\lambda}_{K^*} = 0, 1\}$. Couplings are independent of each other because of parity violation in weak decays. The strong $K^* \to K^-\pi^+$ decay amplitude is

$$\mathcal{A}^{K^*\to K^-\pi^+}_{\bar{\lambda}_{K^*}} = \mathcal{H}^{K^*\to K^-\pi^+}_{0,0} d^{*J_{K^*}}_{\bar{\lambda}_{K^*},0}(\bar{\theta}_K)\mathcal{R}(m^2_{K^-\pi^+}), \tag{A14}$$

where $\mathcal{R}(m^2_{K^-\pi^+})$ is the line shape of the K^* resonance and $\bar{\theta}_K$ is the kaon momentum signed polar angle in the K^* opposite-helicity coordinate system,

$$\bar{\theta}_K = \arctan\left(p_x^{K^*}(K^-), p_z^{K^*}(K^-)\right). \tag{A15}$$

Signed polar angles are used as helicity angles in order to have rotations only around the y axis of the decay plane system. Otherwise, the use of positive polar angles would require additional azimuthal rotations around the z axis (to flip the y axis direction) complicating unnecessarily the expression of the helicity amplitudes. In the amplitude fit the coupling $\mathcal{H}^{K^*\to K^-\pi^+}_{0,0}$ cannot be determined independently of $\mathcal{H}^{\Lambda_c^+\to K^*p}_{m_p,\bar{\lambda}_{K^*}}$ couplings, therefore it is set equal to 1 and absorbed into the latter.

Considering the $\Lambda_c^+ \to \Lambda(\to pK^-)\pi^+$ decay chain, the $\Lambda_c^+ \to \Lambda\pi^+$ decay amplitude is

$$\mathcal{A}^{\Lambda_c^+\to\Lambda\pi^+}_{\nu_{\Lambda_c^+},\lambda_\Lambda} = \mathcal{H}^{\Lambda_c^+\to\Lambda\pi^+}_{\lambda_\Lambda,0} d^{1/2}_{\nu_{\Lambda_c^+},\lambda_\Lambda}(\theta_\Lambda), \tag{A16}$$

in which λ_Λ is the Λ helicity reached from the Λ_c^+ system and θ_Λ is the signed polar angle of the Λ momentum in the DP system,

$$\theta_\Lambda = \arctan\left(p_x^{\Lambda_c^+}(\Lambda), p_z^{\Lambda_c^+}(\Lambda)\right). \tag{A17}$$

The angular momentum conservation relations in Eq. (A6) allow two helicity couplings, $\lambda_\Lambda = \pm 1/2$, to fit for each resonance whatever J_Λ is.

The $\Lambda \to pK^-$ decay amplitude is

$$\mathcal{A}^{\Lambda\to pK^-}_{\lambda_\Lambda,\lambda_p^\Lambda} = \mathcal{H}^{\Lambda\to pK^-}_{\lambda_p^\Lambda,0} d^{J_\Lambda}_{\lambda_\Lambda,\lambda_p^\Lambda}(\theta_p^\Lambda)\mathcal{R}(m^2_{pK^-}), \tag{A18}$$

where λ_p^Λ is the proton helicity, θ_p^Λ the proton signed polar angle, both defined in the helicity coordinate system reached from the Λ resonance frame, while $\mathcal{R}(m^2_{pK^-})$ is the line shape of the Λ resonance. The two helicity couplings corresponding to $\lambda_p^\Lambda = \pm 1/2$ are related by Eq. (A7) thanks to parity conservation in strong interactions,

$$\mathcal{H}^{\Lambda\to pK^-}_{-\lambda_p^\Lambda,0} = -P_\Lambda(-1)^{J_\Lambda - 1/2}\mathcal{H}^{\Lambda\to pK^-}_{\lambda_p^\Lambda,0}, \tag{A19}$$

with P_Λ the parity of the Λ resonance, and the proton and kaon parities $P_p = 1$, $P_K = -1$ have been inserted. In the amplitude fit these couplings cannot be determined independently of $\mathcal{H}^{\Lambda_c^+\to\Lambda\pi^+}_{\lambda_\Lambda,0}$ couplings, so they are absorbed into the latter setting them as $\mathcal{H}^{\Lambda\to pK^-}_{+1/2,0} = 1$ and $\mathcal{H}^{\Lambda\to pK^-}_{-1/2,0} = -P_\Lambda(-1)^{J_\Lambda - 1/2}$, with zero imaginary parts.

The matching of proton spin states from the Λ helicity system to the canonical system is performed applying the method of Ref. [38]. The transformation sequence applied to reach the proton helicity system is undone step by step in order to ensure a consistent phase definition of fermion spin states. Three rotations must be applied: two of angles θ_p^Λ and θ_Λ, plus the Wigner rotation accounting for the different boost sequence applied to reach the two systems. The Wigner rotation can be written in angle-axis decomposition [66], obtained in terms of gamma factors $\gamma^S_{S'}$ and boost vectors $\boldsymbol{u}^S_{S'}$ associated to Lorentz transformations connecting S to S' reference frames. The Wigner rotation has angle

$$\alpha_\Lambda^W = \arccos\left[\frac{\left(1+\gamma_p^{\Lambda_c^+}+\gamma_\Lambda^{\Lambda_c^+}+\gamma_p^\Lambda\right)^2}{(1+\gamma_p^{\Lambda_c^+})(1+\gamma_\Lambda^{\Lambda_c^+})(1+\gamma_p^\Lambda)} - 1\right], \tag{A20}$$

and axis,

$$\boldsymbol{a}_\Lambda^W = \frac{\boldsymbol{u}_\Lambda^{\Lambda_c^+} \times \boldsymbol{u}_p^\Lambda}{|\boldsymbol{u}_\Lambda^{\Lambda_c^+} \times \boldsymbol{u}_p^\Lambda|} = \hat{\boldsymbol{y}}_{\mathrm{DP}}, \tag{A21}$$

which coincides with the y axis of the decay plane coordinate system. All these rotations are around the same y axis, so they can be combined into just one rotation $R_y(\theta_p^\Lambda + \theta_\Lambda + \alpha_\Lambda^W)$, represented by $d^{1/2}_{m_p,\lambda_p^\Lambda}(\theta_p^\Lambda + \theta_\Lambda + \alpha_\Lambda^W)$.

The amplitude associated to the $\Lambda_c^+ \to \Delta^{++}(\to p\pi^+)K^-$ decay chain is similar to the Λ one, having the same spin structure. The $\Lambda_c^+ \to \Delta^{++}K^-$ decay amplitude is

$$\mathcal{A}^{\Lambda_c^+\to\Delta^{++}K^-}_{\nu_{\Lambda_c^+},\lambda_\Delta} = \mathcal{H}^{\Lambda_c^+\to\Delta^{++}K^-}_{\lambda_\Delta,0} d^{1/2}_{\nu_{\Lambda_c^+},\lambda_\Delta}(\theta_\Delta), \quad \text{(A22)}$$

with λ_Δ the Δ helicity and θ_Δ the signed polar angle of the Δ momentum in the DP system. Two helicity couplings corresponding to $\lambda_\Delta = \pm 1/2$ are allowed for each resonance. The $\Delta^{++} \to p\pi^+$ decay amplitude is

$$\mathcal{A}^{\Delta^{++}\to p\pi^+}_{\lambda_\Delta,\lambda_p^\Delta} = \mathcal{H}^{\Delta^{++}\to p\pi^+}_{\lambda_p^\Delta,0} d^{J_\Delta}_{\lambda_\Delta,\lambda_p^\Delta}(\theta_p^\Delta)\mathcal{R}(m^2_{p\pi^+}), \quad \text{(A23)}$$

with λ_p^Δ the proton helicity and θ_p^Δ the signed polar angle, both defined in the Δ helicity system. The strong decay couplings are absorbed into $\mathcal{H}^{\Lambda_c^+\to\Delta^{++}K^-}_{\lambda_\Delta,0}$ setting them to $\mathcal{H}^{\Delta^{++}\to p\pi^+}_{+1/2,0} = 1$ and $\mathcal{H}^{\Delta^{++}\to p\pi^+}_{-1/2,0} = -P_\Delta(-1)^{J_\Delta - 1/2}$.

The matching of proton spin states from the Δ helicity system to the canonical system is performed similarly to the Λ decay chain. The Wigner rotation angle is

$$\alpha_\Delta^W = \arccos\left[\frac{(1+\gamma_p^{\Lambda_c^+}+\gamma_\Delta^{\Lambda_c^+}+\gamma_p^\Delta)^2}{(1+\gamma_p^{\Lambda_c^+})(1+\gamma_\Delta^{\Lambda_c^+})(1+\gamma_p^\Delta)} - 1\right], \quad \text{(A24)}$$

around the axis

$$\boldsymbol{a}_\Delta^W = \frac{\boldsymbol{u}_\Delta^{\Lambda_c^+} \times \boldsymbol{u}_p^\Delta}{|\boldsymbol{u}_\Delta^{\Lambda_c^+} \times \boldsymbol{u}_p^\Delta|} = -\hat{\mathbf{y}}_{\mathrm{DP}}, \quad \text{(A25)}$$

which is opposite to the y axis of the decay plane coordinate system. Therefore, the proton spin rotation can be written as $R_y(\theta_p^\Delta + \theta_\Delta - \alpha_\Delta^W)$, with reversed Wigner angle sign.

The decay amplitude for each intermediate helicity state is the product of the two two-body decay amplitudes in which the three-body decay is decomposed, summed over the allowed helicity states for each resonant contribution. For the Λ and Δ^{++} decay chains the amplitude is further multiplied by the Wigner d-matrices representing the spin matching rotation and summed over proton helicities,

$$\begin{aligned}
\mathcal{A}^{K^*}_{\nu_{\Lambda_c^+},m_p} &= \sum_{\bar\lambda_{K^*}} \mathcal{H}^{\Lambda_c^+\to pK^*}_{m_p,\bar\lambda_{K^*}} \delta_{\nu_{\Lambda_c^+},m_p+\bar\lambda_{K^*}} d^{*J_{K^*}}_{\bar\lambda_{K^*},0}(\bar\theta_K)\mathcal{R}(m^2_{K^-\pi^+}),\\
\mathcal{A}^{\Lambda}_{\nu_{\Lambda_c^+},m_p} &= \sum_{\lambda_\Lambda}\sum_{\lambda_p^\Lambda} d^{1/2}_{m_p,\lambda_p^\Lambda}(\theta_p^\Lambda + \theta_\Lambda + \alpha_\Lambda^W)\mathcal{H}^{\Lambda_c^+\to\Lambda\pi^+}_{\lambda_\Lambda,0}\\
&\quad\times \mathcal{H}^{\Lambda\to pK^-}_{\lambda_p^\Lambda,0} d^{1/2}_{\nu_{\Lambda_c^+},\lambda_\Lambda}(\theta_\Lambda) d^{J_\Lambda}_{\lambda_\Lambda,\lambda_p^\Lambda}(\theta_p^\Lambda)\mathcal{R}(m^2_{pK^-}),\\
\mathcal{A}^{\Delta^{++}}_{\nu_{\Lambda_c^+},m_p} &= \sum_{\lambda_{\Delta^{++}}}\sum_{\lambda_p^\Delta} d^{1/2}_{m_p,\lambda_p^\Delta}(\theta_p^\Delta + \theta_\Delta - \alpha_\Delta^W)\mathcal{H}^{\Lambda_c^+\to\Delta^{++}K^-}_{\lambda_\Delta,0}\\
&\quad\times \mathcal{H}^{\Delta^{++}\to p\pi^+}_{\lambda_p^\Delta,0} d^{1/2}_{\nu_{\Lambda_c^+},\lambda_\Delta}(\theta_\Delta) d^{J_\Delta}_{\lambda_\Delta,\lambda_p^\Delta}(\theta_p^\Delta)\mathcal{R}(m^2_{p\pi^+}).
\end{aligned} \quad \text{(A26)}$$

The total amplitude for the $\Lambda_c^+ \to pK^-\pi^+$ decay is obtained summing the amplitudes for the different intermediate states,

$$\begin{aligned}
\mathcal{O}_{\nu_{\Lambda_c^+},m_p}(m^2_{pK^-}, m^2_{K^-\pi^+}) &= \sum_{i=1}^{N_{K^*}} \mathcal{A}^{K_i^*}_{\nu_{\Lambda_c^+},m_p} + \sum_{j=1}^{N_\Lambda} \mathcal{A}^{\Lambda_i^*}_{\nu_{\Lambda_c^+},m_p}\\
&\quad + \sum_{k=1}^{N_{\Delta^{++}}} \mathcal{A}^{\Delta_k^{*++}}_{\nu_{\Lambda_c^+},m_p}.
\end{aligned} \quad \text{(A27)}$$

Fit fractions, FF, for each resonance R are obtained by computing the integral of the amplitude model over the phase space where only the R contribution is left. Fit fractions are normalized to the complete amplitude model integral,

$$FF = \frac{\int d\Omega \sum_{m_{\Lambda_c^+},m_p} |\mathcal{A}^R_{m_{\Lambda_c^+},m_p}(\Omega)|^2}{\int d\Omega \sum_{m_{\Lambda_c^+},m_p} |\mathcal{A}_{m_{\Lambda_c^+},m_p}(\Omega)|^2}. \quad \text{(A28)}$$

3. Polarized decay rate

A generic polarization state of the Λ_c^+ baryon is described by the spin-1/2 density matrix

$$\rho^{\Lambda_c^+} = \frac{1}{2}(\mathbb{I} + \boldsymbol{P}\cdot\boldsymbol{\sigma}) = \frac{1}{2}\begin{pmatrix} 1+P_z & P_x - iP_y \\ P_x + iP_y & 1-P_z \end{pmatrix}, \quad \text{(A29)}$$

where P_x, P_y and P_z are the components of the polarization vector $\boldsymbol{P}$ in the polarization system (see definition in Sec. A 1) and $\boldsymbol{\sigma}$ are the three Pauli matrices. The differential decay rate for a $\Lambda_c^+ \to pK^-\pi^+$ decay with a generic Λ_c^+ polarization is

$$\begin{aligned}
p(\Omega, \boldsymbol{P}) = &\sum_{m_{\Lambda_c^+}=-1/2}^{1/2}\sum_{m'_{\Lambda_c^+}=-1/2}^{1/2}\sum_{m_p=-1/2}^{1/2} (\rho^{\Lambda_c^+})_{m_{\Lambda_c^+},m'_{\Lambda_c^+}}\\
&\times \mathcal{A}_{m'_{\Lambda_c^+},m_p}(\Omega)\mathcal{A}^*_{m_{\Lambda_c^+},m_p}(\Omega),
\end{aligned} \quad \text{(A30)}$$

in which proton spin states are summed over since the proton polarization is not measured. Substituting the Λ_c^+ density matrix expression, the differential rate takes the form

$$p(\Omega, \boldsymbol{P}) = \frac{1}{\mathcal{N}} \sum_{m_p=\pm 1/2} \{(1+P_z)|\mathcal{A}_{1/2,m_p}(\Omega)|^2 + (1-P_z)|\mathcal{A}_{-1/2,m_p}(\Omega)|^2 + 2\mathrm{Re}[(P_x - iP_y)\mathcal{A}^*_{1/2,m_p}(\Omega)\mathcal{A}_{-1/2,m_p}(\Omega)]\}, \tag{A31}$$

where $\mathcal{N}$ is a normalization constant introduced to make p a probability density function.

APPENDIX B: ROTATION OF REFERENCE SYSTEMS AND SPIN STATES

The rotation of an initial Cartesian reference frame (x, y, z) into a final one (X, Y, Z) can be described by a Euler rotation parametrized by three angles α, β, γ. Taking the $z-y-z$ convention for the rotation axes, the Euler rotation is composed by a first rotation of angle α around the z axis, a second rotation of angle β around the rotated y' axis and a third one of angle γ around the twice rotated z'' axis,

$$\mathcal{R}(\alpha,\beta,\gamma) = R_{z''}(\gamma)R_{y'}(\beta)R_z(\alpha) = e^{-i\gamma\hat{J}_{z''}}e^{-i\beta\hat{J}_{y'}}e^{-i\alpha\hat{J}_z}. \tag{B1}$$

The latter equality expresses rotations in terms of the generating angular momentum operators. Here, active rotations are considered, in which the normalized vectors $\hat{\boldsymbol{x}}, \hat{\boldsymbol{y}}, \hat{\boldsymbol{z}}$ defining the initial reference frame are actively rotated to those describing the final reference frame $\hat{\boldsymbol{X}}, \hat{\boldsymbol{Y}}, \hat{\boldsymbol{Z}}$,

$$\hat{\boldsymbol{X}}^i = \mathcal{R}(\alpha,\beta,\gamma)\hat{\boldsymbol{x}}^i. \tag{B2}$$

The three Euler angles can be computed as follows: given the vector $\boldsymbol{N} = \hat{\boldsymbol{z}} \times \hat{\boldsymbol{Z}}$, α is the angle between $\hat{\boldsymbol{y}}$ and $\hat{\boldsymbol{N}}$, β is the angle between $\hat{\boldsymbol{z}}$ and $\hat{\boldsymbol{Z}}$ axes, and γ is the angle between $\hat{\boldsymbol{N}}$ and $\hat{\boldsymbol{Y}}$ axes. In formulas,

$$\begin{aligned} \alpha &= \arctan(\hat{\boldsymbol{y}}\cdot\hat{\boldsymbol{Z}}, \hat{\boldsymbol{x}}\cdot\hat{\boldsymbol{Z}}) \in [-\pi,\pi], \\ \beta &= \arccos(\hat{\boldsymbol{z}}\cdot\hat{\boldsymbol{Z}}) \in [0,\pi], \\ \gamma &= \arctan(\hat{\boldsymbol{z}}\cdot\hat{\boldsymbol{Y}}, -\hat{\boldsymbol{z}}\cdot\hat{\boldsymbol{X}}) \in [-\pi,\pi]. \end{aligned} \tag{B3}$$

The Euler rotation can be also expressed in terms of rotations around the initial reference frame axes only, by means of the equality

$$\mathcal{R}(\alpha,\beta,\gamma) = R_z(\alpha)R_y(\beta)R_z(\gamma) = e^{-i\alpha\hat{J}_z}e^{-i\beta\hat{J}_y}e^{-i\gamma\hat{J}_z}. \tag{B4}$$

The action of the rotation operators $\mathcal{R}(\alpha,\beta,\gamma)$ on angular momentum eigenstates $|J,m\rangle$ can be written as

$$\mathcal{R}(\alpha,\beta,\gamma)|J,m\rangle = \sum_{m'=-J}^{J} D^J_{m',m}(\alpha,\beta,\gamma)|J,m'\rangle, \tag{B5}$$

where the Wigner D-matrices $D^J_{m'm}(\alpha,\beta,\gamma)$ are the matrix elements of the rotation operator in the given spin reference frame,

$$D^J_{m',m}(\alpha,\beta,\gamma) = \langle J,m'|\mathcal{R}(\alpha,\beta,\gamma)|J,m\rangle. \tag{B6}$$

From the latter equality of Eq. (B4), the Wigner D-matrices can be factorized as

$$\begin{aligned} D^J_{m',m}(\alpha,\beta,\gamma) &= \langle J,m'|e^{-i\alpha\hat{J}_z}e^{-i\beta\hat{J}_y}e^{-i\gamma\hat{J}_z}|J,m\rangle \\ &= e^{-im'\alpha}d^J_{m',m}(\beta)e^{-im\gamma}, \end{aligned} \tag{B7}$$

where the Wigner d-matrix elements are known combinations of trigonometric functions of β depending on the parameters J, m and m'.

APPENDIX C: EFFICIENCY AND BACKGROUND MODELS

Efficiency and background models are obtained using factorized Legendre polynomial expansions over the decay phase space. To this end, the five phase-space variables are transformed into new variables defined in the range $[-1, 1]$. The mass variables $m^2_{pK^-}$ and $m^2_{K^-\pi^+}$ are replaced by the so-called square Dalitz plot variables,

$$\begin{aligned} m'_{pK^-} &= 2\frac{m_{pK^-} - m^{\min}_{pK^-}}{m^{\max}_{pK^-} - m^{\min}_{pK^-}} - 1, \\ \cos\theta^{\Lambda^*}_{K\pi} &= \frac{m^2_{K^-} + m^2_{\pi^+} + 2E_{K^-}E_{\pi^+} - m^2_{pK^-}}{2p_{K^-}p_{\pi^+}}, \end{aligned} \tag{C1}$$

where $m^{\min}_{pK^-} = m_p + m_{K^-}$ and $m^{\max}_{pK^-} = m_{\Lambda_c^+} - m_{\pi^+}$ are the minimum and maximum pK^- invariant mass allowed values, and $\cos\theta^{\Lambda^*}_{K\pi}$ is the cosine of the angle between the kaon and the pion in the Λ rest frame. The transformation of the decay plane orientation variables is simple, $\cos\theta'_p = \cos\theta_p$, $\phi'_p = \phi_p/\pi$ and $\chi' = \chi/\pi$.

Exploiting the completeness and orthogonality of Legendre polynomials, a generic function f over a phase-space variable x is expanded as

$$f(x) = \sum_i c_i L(x,i),$$
$$c_i = \sum_{n=0}^{N} \frac{w_n}{\rho(x)} (2i+1) L(x,i), \tag{C2}$$

where $L(x,l)$ is the Legendre polynomial of order l, w_n is the weight associated to the phase-space point, for simulated events only, and ρ represents the nonuniformity of the phase-space density over the m'_{pK^-} variable.

Both parametrizations are obtained by building five one-dimensional polynomial expansions multiplied together,

$$f(\Omega) = f(m'_{pK^-}) f(\cos\theta^{\Lambda^*}_{K\pi}) f(\cos\theta'_p) f(\phi'_p) f(\chi'), \tag{C3}$$

with correlations among phase-space variables found to be negligible.

The efficiency parametrization $\epsilon(\Omega)$ is derived from simulated $\Lambda_c^+ \to pK^-\pi^+$ events generated uniformly in phase space, while the background parametrization $p_{\rm bkg}(\Omega)$ is obtained from data candidates selected in the invariant mass sidebands within 40 and 80 MeV from the known Λ_c^+ mass [25].

APPENDIX D: BREIT-WIGNER LINE SHAPE

To reproduce the typical suppression of transitions involving nonzero orbital angular momentum, a mass-dependent width is introduced in the Breit-Wigner parametrization, the latter multiplied by angular barrier terms involving Blatt-Weisskopf form factors [67,68],

$$\mathcal{R}_{\rm BW}(m^2) = \left[\frac{q(m)}{q_0}\right]^{L_{\Lambda_c^+}} \left[\frac{p(m)}{p_0}\right]^{L_R} \frac{F_{\Lambda_c^+}(m, L_{\Lambda_c^+}) F_R(m, L_R)}{m_0^2 - m^2 - i m_0 \Gamma(m)}, \tag{D1}$$

where the mass-dependent width,

$$\Gamma(m) = \Gamma_0 \left[\frac{p(m)}{p_0}\right]^{2L_R+1} \frac{m_0}{m} F_R^2(m, L_R), \tag{D2}$$

is introduced. The definition of the different quantities entering the above expressions are the following: m is the invariant mass of the resonance, m_0 and Γ_0 are its Breit-Wigner mass and width, $p(m)$ is the momentum of one of the decay products in the resonance two-body decay, $p_0 \equiv p(m_0)$, $q(m)$ is the momentum of one of the decay products in the Λ_c^+ two-body decay $\Lambda_c^+ \to Rh$, $q_0 = q(m_0)$, both defined in the rest frame of the decaying particle, $L_{\Lambda_c^+}$ and L_R are the orbital angular momenta associated to the Λ_c^+ and R decays, respectively. The Blatt-Weisskopf form factors for the resonance, $F_R(m, L_R)$, and for the Λ_c^+, $F_{\Lambda_c^+}(m, L_{\Lambda_c^+})$, are parametrized as

$$F_{R,\Lambda_c^+}(m,L) = \begin{cases} 1 & L=0 \\ \sqrt{\frac{1+z_0^2}{1+z^2(m)}} & L=1 \\ \sqrt{\frac{9+3z_0^2+z_0^4}{9+3z^2(m)+z^4(m)}} & L=2, \end{cases} \tag{D3}$$

in which the definitions of the terms $z(m)$ and z_0 depend on whether the form factor for the resonance R or for the Λ_c^+ is being considered. For R these terms are given by $z(m) = p(m)d$ and $z_0 = p_0 d$, where $p(m)$ is the momentum of one of the decay products in the resonance two-body decay, $p_0 \equiv p(m_0)$, and d is a radial parameter taken to be 1.5 GeV^{-1}. The angular barrier factors arise from the nonrelativistic quantization of a particle in a radial potential, and d is often interpreted as the radius of the resonance. For the Λ_c^+ baryon the respective functions are $z(m) = q(m)d$ and $z_0 = q_0 d$, in which $q(m)$ is the momentum of one of the decay products in the Λ_c^+ two-body decay $\Lambda_c^+ \to Rh$, $q_0 = q(m_0)$, and $d = 5.0$ GeV^{-1}.

The mass-dependent width and the form factors depend on the orbital angular momenta of the two-body decays. For the Λ_c^+ weak decay, the orbital angular momentum is not constrained: the minimum possible value is assumed, since one can expect higher assignments to be energetically disfavored. For half-integer spin Λ and Δ^{++} resonances it is $L_{\Lambda_c^+} = J_R - 1/2$, J_R being the resonance spin, it is $L_{\Lambda_c^+} = 0$ for spin-zero K^* resonances and $L_{\Lambda_c^+} = J_R - 1$ for higher-spin K^* resonances. A fit performed using LS couplings instead of helicity couplings, including higher orbital angular momentum states, is considered as an alternative model (Sec. V). For the strong decay of Λ and Δ^{++} resonances, the orbital angular momentum L_R is determined by the conservation of angular momentum, which requires $L_R = J_R \pm 1/2$, and the parity of the resonance, $P_R = -(-1)^{L_R}$, which chooses one of the L_R values. The additional minus sign is given by the negative parity of the final-state meson. For K^* resonances decaying into two mesons, the orbital angular momentum is $L_R = J_R$.

[1] D. Marangotto, Extracting maximum information from polarised baryon decays via amplitude analysis: The $\Lambda_c^+ \to pK^-\pi^+$ case, Adv. High Energy Phys. **2020**, 7463073 (2020).

[2] J. G. Körner and M. Krämer, Exclusive nonleptonic charm baryon decays, Z. Phys. C **55**, 659 (1992).

[3] M. Davier, L. Duflot, F. Le Diberder, and A. Rouge, The optimal method for the measurement of tau polarization, Phys. Lett. B **306**, 411 (1993).

[4] B. König, J. G. Körner, M. Krämer, and P. Kroll, Infinite momentum frame calculation of semileptonic heavy $\Lambda_b \to \Lambda_c$ transitions including HQET improvements, Phys. Rev. D **56**, 4282 (1997).

[5] M. Pervin, W. Roberts, and S. Capstick, Semileptonic decays of heavy lambda baryons in a quark model, Phys. Rev. C **72**, 035201 (2005).

[6] T. Gutsche, M. A. Ivanov, J. G. Körner, V. E. Lyubovitskij, P. Santorelli, and N. Habyl, Semileptonic decay $\Lambda_b \to \Lambda_c \tau^- \bar{\nu}_\tau$ in the covariant confined quark model, Phys. Rev. D **91**, 074001 (2015); **91**, 119907(E) (2015).

[7] S. Shivashankara, W. Wu, and A. Datta, $\Lambda_b \to \Lambda_c \tau \bar{\nu}_\tau$ decay in the Standard Model and with new physics, Phys. Rev. D **91**, 115003 (2015).

[8] R. Dutta, $\Lambda_b \to (\Lambda_c, p)\tau\nu$ decays within Standard Model and beyond, Phys. Rev. D **93**, 054003 (2016).

[9] R. N. Faustov and V. O. Galkin, Semileptonic decays of Λ_b baryons in the relativistic quark model, Phys. Rev. D **94**, 073008 (2016).

[10] X.-Q. Li, Y.-D. Yang, and X. Zhang, $\Lambda_b \to \Lambda_c \tau \bar{\nu}_\tau$ decay in scalar and vector leptoquark scenarios, J. High Energy Phys. 02 (2017) 068.

[11] A. Celis, M. Jung, X.-Q. Li, and A. Pich, Scalar contributions to $b \to c(u)\tau\nu$ transitions, Phys. Lett. B **771**, 168 (2017).

[12] A. Datta, S. Kamali, S. Meinel, and A. Rashed, Phenomenology of $\Lambda_b \to \Lambda_c \tau \bar{\nu}_\tau$ using lattice QCD calculations, J. High Energy Phys. 08 (**2017**) 131.

[13] J. Zhu *et al.*, Probing the R-parity violating supersymmetric effects in $B_c \to J/\psi \ell^- \bar{\nu}_\ell, \eta_c \ell^- \bar{\nu}_\ell$ and $\Lambda_b \to \Lambda_c \ell^- \bar{\nu}_\ell$ decays, Nucl. Phys. **B934**, 380 (2018).

[14] E. Di Salvo, F. Fontanelli, and Z. J. Ajaltouni, Detailed study of the decay $\Lambda_b \to \Lambda_c \tau \bar{\nu}_\tau$, Int. J. Mod. Phys. A **33**, 1850169 (2018).

[15] A. Ray, S. Sahoo, and R. Mohanta, Probing new physics in semileptonic Λ_b decays, Phys. Rev. D **99**, 015015 (2019).

[16] F. U. Bernlochner, Z. Ligeti, D. J. Robinson, and W. L. Sutcliffe, Precise predictions for $\Lambda_b \to \Lambda_c$ semileptonic decays, Phys. Rev. D **99**, 055008 (2019).

[17] N. Penalva, E. Hernández, and J. Nieves, Further tests of lepton flavour universality from the charged lepton energy distribution in $b \to c$ semileptonic decays: The case of $\Lambda_b \to \Lambda_c \ell \bar{\nu}_\ell$, Phys. Rev. D **100**, 113007 (2019).

[18] Q.-Y. Hu, X.-Q. Li, Y.-D. Yang, and D.-H. Zheng, The measurable angular distribution of $\Lambda_b^0 \to \Lambda_c^+(\to \Lambda^0 \pi^+) \times \tau^-(\to \pi^- \nu_\tau)\bar{\nu}_\tau$ decay, J. High Energy Phys. 02 (2021) 183.

[19] J. P. Lees *et al.* (*BABAR* Collaboration), Measurement of an excess of $\bar{B} \to D^{(*)} \tau^- \bar{\nu}_\tau$ decays and implications for charged Higgs bosons, Phys. Rev. D **88**, 072012 (2013).

[20] M. Huschle *et al.* (Belle Collaboration), Measurement of the branching ratio of $\bar{B} \to D^{(*)} \tau^- \bar{\nu}_\tau$ relative to $\bar{B} \to D^{(*)} \ell^- \bar{\nu}_\ell$ decays with hadronic tagging at Belle, Phys. Rev. D **92**, 072014 (2015).

[21] Y. Sato *et al.* (Belle Collaboration), Measurement of the branching ratio of $\bar{B}^0 \to D^{*+} \tau^- \bar{\nu}_\tau$ relative to $\bar{B}^0 \to D^{*+} \ell^- \bar{\nu}_\ell$ decays with a semileptonic tagging method, Phys. Rev. D **94**, 072007 (2016).

[22] S. Hirose *et al.* (Belle Collaboration), Measurement of the τ Lepton Polarization and $R(D^*)$ in the Decay $\bar{B} \to D^* \tau^- \bar{\nu}_\tau$, Phys. Rev. Lett. **118**, 211801 (2017).

[23] R. Aaij *et al.* (LHCb Collaboration), Test of lepton flavor universality by the measurement of the $B^0 \to D^{*-} \tau^+ \nu_\tau$ branching fraction using three-prong τ decays, Phys. Rev. D **97**, 072013 (2018).

[24] R. Aaij *et al.* (LHCb Collaboration), Measurement of the Ratio of Branching Fractions $\mathcal{B}(\bar{B}^0 \to D^{*+} \tau^- \bar{\nu}_\tau)/\mathcal{B}(\bar{B}^0 \to D^{*+} \mu^- \bar{\nu}_\mu)$, Phys. Rev. Lett. **115**, 111803 (2015); **115**, 159901(E) (2015).

[25] P. A. Zyla *et al.* (Particle Data Group), Review of particle physics, Prog. Theor. Exp. Phys. **2020**, 083C01 (2020).

[26] B. König, J. G. Körner, and M. Krämer, On the determination of the $b \to c$ handedness using nonleptonic Λ_c decays, Phys. Rev. D **49**, 2363 (1994).

[27] X.-L. Mu, Y. Li, Z.-T. Zou, and B. Zhu, Investigation of effects of new physics in $\Lambda_b \to \Lambda_c \tau \bar{\nu}_\tau$ decay, Phys. Rev. D **100**, 113004 (2019).

[28] A. F. Falk and M. E. Peskin, Production, decay, and polarization of excited heavy hadrons, Phys. Rev. D **49**, 3320 (1994).

[29] M. Galanti, A. Giammanco, Y. Grossman, Y. Kats, E. Stamou, and J. Zupan, Heavy baryons as polarimeters at colliders, J. High Energy Phys. 11 (2015) 067.

[30] G. R. Goldstein, Polarization of inclusively produced Λ_c^+ in a QCD based hybrid model, arXiv:hep-ph/9907573.

[31] G. R. Goldstein and S. Liuti, Angular momentum and polarization in hadron collisions up to LHC energies, Int. J. Mod. Phys. Conf. Ser. **37**, 1560038 (2015).

[32] T. Mannel and G. A. Schuler, Semileptonic decays of bottom baryons at LEP, Phys. Lett. B **279**, 194 (1992).

[33] F. J. Botella, L. M. Garcia Martin, D. Marangotto, F. Martinez Vidal, A. Merli, N. Neri, A. Oyanguren, and J. Ruiz Vidal, On the search for the electric dipole moment of strange and charm baryons at LHC, Eur. Phys. J. C **77**, 181 (2017).

[34] E. Bagli *et al.*, Electromagnetic dipole moments of charged baryons with bent crystals at the LHC, Eur. Phys. J. C **77**, 828 (2017).

[35] D. Marangotto, Amplitude analysis and polarisation measurement of the Λ_c^+ baryon in $pK^-\pi^+$ final state for electromagnetic dipole moment experiment, Ph.D. thesis, Università degli studi di Milano, 2020, https://cds.cern.ch/record/2713231.

[36] S. Aiola, L. Bandiera, G. Cavoto, F. De Benedetti, J. Fu, V. Guidi *et al.*, Progress towards the first measurement of charm baryon dipole moments, Phys. Rev. D **103**, 072003 (2021).

[37] E. M. Aitala *et al.* (E791 Collaboration), Multidimensional resonance analysis of $\Lambda_c^+ \to pK^-\pi^+$, Phys. Lett. B **471**, 449 (2000).

[38] D. Marangotto, Helicity amplitudes for generic multibody particle decays featuring multiple decay chains, Adv. High Energy Phys. **2020**, 6674595 (2020).

[39] A. A. Alves Jr. *et al.* (LHCb Collaboration), The LHCb detector at the LHC, J. Instrum. **3**, S08005 (2008).

[40] R. Aaij *et al.* (LHCb Collaboration), LHCb detector performance, Int. J. Mod. Phys. A **30**, 1530022 (2015).

[41] V. V. Gligorov and M. Williams, Efficient, reliable and fast high-level triggering using a bonsai boosted decision tree, J. Instrum. **8**, P02013 (2013).

[42] T. Likhomanenko, P. Ilten, E. Khairullin, A. Rogozhnikov, A. Ustyuzhanin, and M. Williams, LHCb topological trigger reoptimization, J. Phys. Conf. Ser. **664**, 082025 (2015).

[43] R. Aaij *et al.* (LHCb Collaboration), Measurements of the Λ_b^0, Ξ_b^-, and Ω_b^- Baryon Masses, Phys. Rev. Lett. **110**, 182001 (2013).

[44] R. Aaij *et al.* (LHCb Collaboration), Precision measurement of D meson mass differences, J. High Energy Phys. 06 (2013) 065.

[45] T. Sjöstrand, S. Mrenna, and P. Skands, A brief introduction to PYTHIA 8.1, Comput. Phys. Commun. **178**, 852 (2008); PYTHIA 6.4 physics and manual, J. High Energy Phys. 05 (2006) 026.

[46] I. Belyaev *et al.*, Handling of the generation of primary events in Gauss, the LHCb simulation framework, J. Phys. Conf. Ser. **331**, 032047 (2011).

[47] D. J. Lange, The EvtGen particle decay simulation package, Nucl. Instrum. Methods Phys. Res., Sect. A **462**, 152 (2001).

[48] N. Davidson, T. Przedzinski, and Z. Was, PHOTOS interface in $C++$: Technical and physics documentation, Comput. Phys. Commun. **199**, 86 (2016).

[49] J. Allison *et al.* (Geant4 Collaboration), Geant4 developments and applications, IEEE Trans. Nucl. Sci. **53**, 270 (2006).Geant4: A simulation toolkit, Nucl. Instrum. Methods Phys. Res., Sect. A **506**, 250 (2003).

[50] M. Clemencic, G. Corti, S. Easo, C. R Jones, S. Miglioranzi, M. Pappagallo, and P. Robbe, The LHCb simulation application, Gauss: Design, evolution and experience, J. Phys. Conf. Ser. **331**, 032023 (2011).

[51] D. Müller, M. Clemencic, G. Corti, and M. Gersabeck, ReDecay: A novel approach to speed up the simulation at LHCb, Eur. Phys. J. C **78**, 1009 (2018).

[52] A. Poluektov, Kernel density estimation of a multidimensional efficiency profile, J. Instrum. **10**, P02011 (2015).

[53] A. Rogozhnikov, Reweighting with boosted decision trees, J. Phys. Conf. Ser. **762**, 012036 (2016).

[54] T. Skwarnicki, A study of the radiative cascade transitions between the Upsilon-prime and Upsilon resonances, Ph.D. thesis, Institute of Nuclear Physics, Krakow, 1986 [Report No. DESY-F31-86-02].

[55] M. Jacob and G. C. Wick, On the general theory of collisions for particles with spin, Ann. Phys. (N.Y.) **7**, 404 (1959).

[56] TensorFlowAnalysis: A collection of useful functions and example scripts for performing amplitude fits using TensorFlow, https://gitlab.cern.ch/poluekt/TensorFlowAnalysis.

[57] M. Abadi *et al.*, TensorFlow: Large-scale machine learning on heterogeneous systems, https://www.tensorflow.org (2015).

[58] F. James and M. Roos, Minuit: A system for function minimization and analysis of the parameter errors and correlations, Comput. Phys. Commun. **10**, 343 (1975).

[59] R. Brun and F. Rademakers, ROOT: An object oriented data analysis framework, Nucl. Instrum. Methods Phys. Res., Sect. A **389**, 81 (1997).

[60] D. V. Bugg, The Kappa in E791 data for $D \to K\pi\pi$, Phys. Lett. B **632**, 471 (2006).

[61] S. M. Flatte, Coupled-channel analysis of the $\pi\eta$ and $K\bar{K}$ systems near $K\bar{K}$ threshold, Phys. Lett. B **63**, 224 (1976).

[62] H. Zhang, J. Tulpan, M. Shrestha, and D. M. Manley, Multichannel parametrization of $\bar{K}N$ scattering amplitudes and extraction of resonance parameters, Phys. Rev. C **88**, 035205 (2013).

[63] W. Cameron *et al.* (Rutherford-London Collaboration), Partial wave analysis of $\bar{K}N \to \bar{K}^*N$ between 1830 MeV and 2170 MeV center-of-mass energy including new data below 1960 MeV, Nucl. Phys. **B146**, 327 (1978).

[64] M. S. Sozzi, Discrete Symmetries and *CP* Violation: From Experiment to Theory, Oxford Graduate Texts (Oxford University Press, New York, New York, 2008).

[65] M. Mikhasenko *et al.* (JPAC Collaboration), Dalitz-plot decomposition for three-body decays, Phys. Rev. D **101**, 034033 (2020).

[66] E. Gourgoulhon, *Special Relativity in General Frames* (Springer, New York, 2013).

[67] J. M. Blatt and V. F. Weisskopf, *Theoretical Nuclear Physics* (Springer, New York, 1952).

[68] F. Von Hippel and C. Quigg, Centrifugal-barrier effects in resonance partial decay widths, shapes, and production amplitudes, Phys. Rev. D **5**, 624 (1972).

R. Aaij,[32] A. S. W. Abdelmotteleb,[50] C. Abellan Beteta,[44] F. Abudinén,[50] T. Ackernley,[54] B. Adeva,[40] M. Adinolfi,[48] H. Afsharnia,[9] C. Agapopoulou,[13] C. A. Aidala,[76] S. Aiola,[25] Z. Ajaltouni,[9] S. Akar,[59] K. Akiba,[32] J. Albrecht,[15] F. Alessio,[42] M. Alexander,[53] A. Alfonso Albero,[39] Z. Aliouche,[56] P. Alvarez Cartelle,[49] S. Amato,[2] J. L. Amey,[48] Y. Amhis,[11,42] L. An,[42] L. Anderlini,[22] M. Andersson,[44] A. Andreianov,[38] M. Andreotti,[21] D. Andreou,[62] D. Ao,[6] F. Archilli,[17] A. Artamonov,[38] M. Artuso,[62] E. Aslanides,[10] M. Atzeni,[44] B. Audurier,[12] S. Bachmann,[17] M. Bachmayer,[43] J. J. Back,[50] A. Bailly-reyre,[13] P. Baladron Rodriguez,[40] V. Balagura,[12] W. Baldini,[21] J. Baptista de Souza Leite,[1] M. Barbetti,[22,k] R. J. Barlow,[56] S. Barsuk,[11] W. Barter,[55] M. Bartolini,[49] F. Baryshnikov,[38] J. M. Basels,[14] G. Bassi,[29,q] B. Batsukh,[4] A. Battig,[15] A. Bay,[43] A. Beck,[50] M. Becker,[15] F. Bedeschi,[29] I. B. Bediaga,[1] A. Beiter,[62] V. Belavin,[38]

S. Belin,[40] V. Bellee,[44] K. Belous,[38] I. Belov,[38] I. Belyaev,[38] G. Bencivenni,[23] E. Ben-Haim,[13] A. Berezhnoy,[38] R. Bernet,[44] D. Berninghoff,[17] H. C. Bernstein,[62] C. Bertella,[56] A. Bertolin,[28] C. Betancourt,[44] F. Betti,[42] Ia. Bezshyiko,[44] S. Bhasin,[48] J. Bhom,[35] L. Bian,[67] M. S. Bieker,[15] N. V. Biesuz,[21] S. Bifani,[47] P. Billoir,[13] A. Biolchini,[32] M. Birch,[55] F. C. R. Bishop,[49] A. Bitadze,[56] A. Bizzeti, M. Bjørn,[57] M. P. Blago,[49] T. Blake,[50] F. Blanc,[43] S. Blusk,[62] D. Bobulska,[53] J. A. Boelhauve,[15] O. Boente Garcia,[40] T. Boettcher,[59] A. Boldyrev,[38] N. Bondar,[38,42] S. Borghi,[56] M. Borsato,[17] J. T. Borsuk,[35] S. A. Bouchiba,[43] T. J. V. Bowcock,[54,42] A. Boyer,[42] C. Bozzi,[21] M. J. Bradley,[55] S. Braun,[60] A. Brea Rodriguez,[40] J. Brodzicka,[35] A. Brossa Gonzalo,[50] D. Brundu,[27] A. Buonaura,[44] L. Buonincontri,[28] A. T. Burke,[56] C. Burr,[42] A. Bursche,[66] A. Butkevich,[38] J. S. Butter,[32] J. Buytaert,[42] W. Byczynski,[42] S. Cadeddu,[27] H. Cai,[67] R. Calabrese,[21,d] L. Calefice,[15,13] S. Cali,[23] R. Calladine,[47] M. Calvi,[26,n] M. Calvo Gomez,[74] P. Camargo Magalhaes,[48] P. Campana,[23] D. H. Campora Perez,[73] A. F. Campoverde Quezada,[6] S. Capelli,[26,n] L. Capriotti,[20,h] A. Carbone,[20,h] G. Carboni,[31] R. Cardinale,[24,l] A. Cardini,[27] I. Carli,[4] P. Carniti,[26,n] L. Carus,[14] A. Casais Vidal,[40] R. Caspary,[17] G. Casse,[54] M. Cattaneo,[42] G. Cavallero,[42] V. Cavallini,[21,j] S. Celani,[43] J. Cerasoli,[10] D. Cervenkov,[57] A. J. Chadwick,[54] M. G. Chapman,[48] M. Charles,[13] Ph. Charpentier,[42] C. A. Chavez Barajas,[54] M. Chefdeville,[8] C. Chen,[3] S. Chen,[4] A. Chernov,[35] S. Chernyshenko,[46] V. Chobanova,[40] S. Cholak,[43] M. Chrzaszcz,[35] A. Chubykin,[38] V. Chulikov,[38] P. Ciambrone,[23] M. F. Cicala,[50] X. Cid Vidal,[40] G. Ciezarek,[42] G. Ciullo,[21,j] P. E. L. Clarke,[52] M. Clemencic,[42] H. V. Cliff,[49] J. Closier,[42] J. L. Cobbledick,[56] V. Coco,[42] J. A. B. Coelho,[11] J. Cogan,[10] E. Cogneras,[9] L. Cojocariu,[37] P. Collins,[42] T. Colombo,[42] L. Congedo,[19,g] A. Contu,[27] N. Cooke,[47] G. Coombs,[53] I. Corredoira,[40] G. Corti,[42] B. Couturier,[42] D. C. Craik,[58] J. Crkovská,[61] M. Cruz Torres,[1,f] R. Currie,[52] C. L. Da Silva,[61] S. Dadabaev,[38] L. Dai,[65] E. Dall'Occo,[15] J. Dalseno,[40] C. D'Ambrosio,[42] A. Danilina,[38] P. d'Argent,[15] J. E. Davies,[56] A. Davis,[56] O. De Aguiar Francisco,[56] J. de Boer,[42] K. De Bruyn,[72] S. De Capua,[56] M. De Cian,[43] U. De Freitas Carneiro Da Graca,[1] E. De Lucia,[23] J. M. De Miranda,[1] L. De Paula,[2] M. De Serio,[19,g] D. De Simone,[44] P. De Simone,[23] F. De Vellis,[15] J. A. de Vries,[73] C. T. Dean,[61] F. Debernardis,[19,g] D. Decamp,[8] V. Dedu,[10] L. Del Buono,[13] B. Delaney,[49] H.-P. Dembinski,[15] V. Denysenko,[44] O. Deschamps,[9] F. Dettori,[27,i] B. Dey,[70] A. Di Cicco,[23] P. Di Nezza,[23] S. Didenko,[38] L. Dieste Maronas,[40] S. Ding,[62] V. Dobishuk,[46] A. Dolmatov,[38] C. Dong,[3] A. M. Donohoe,[18] F. Dordei,[27] A. C. dos Reis,[1] L. Douglas,[53] A. G. Downes,[8] M. W. Dudek,[35] L. Dufour,[42] V. Duk,[71] P. Durante,[42] J. M. Durham,[61] D. Dutta,[56] A. Dziurda,[35] A. Dzyuba,[38] S. Easo,[51] U. Egede,[63] V. Egorychev,[38] S. Eidelman,[38,a] S. Eisenhardt,[52] S. Ek-In,[43] L. Eklund,[75] S. Ely,[62] A. Ene,[37] E. Epple,[61] S. Escher,[14] J. Eschle,[44] S. Esen,[44] T. Evans,[56] L. N. Falcao,[1] Y. Fan,[6] B. Fang,[67] S. Farry,[54] D. Fazzini,[26,n] M. Feo,[42] A. D. Fernez,[60] F. Ferrari,[20] L. Ferreira Lopes,[43] F. Ferreira Rodrigues,[2] S. Ferreres Sole,[32] M. Ferrillo,[44] M. Ferro-Luzzi,[42] S. Filippov,[38] R. A. Fini,[19] M. Fiorini,[21,j] M. Firlej,[34] K. M. Fischer,[57] D. S. Fitzgerald,[76] C. Fitzpatrick,[56] T. Fiutowski,[34] F. Fleuret,[12] M. Fontana,[13] F. Fontanelli,[24,l] R. Forty,[42] D. Foulds-Holt,[49] V. Franco Lima,[54] M. Franco Sevilla,[60] M. Frank,[42] E. Franzoso,[21,j] G. Frau,[17] C. Frei,[42] D. A. Friday,[53] J. Fu,[6] Q. Fuehring,[15] E. Gabriel,[32] G. Galati,[19,g] A. Gallas Torreira,[40] D. Galli,[20,h] S. Gambetta,[52,42] Y. Gan,[3] M. Gandelman,[2] P. Gandini,[25] Y. Gao,[5] M. Garau,[27,i] L. M. Garcia Martin,[50] P. Garcia Moreno,[39] J. García Pardiñas,[26,n] B. Garcia Plana,[40] F. A. Garcia Rosales,[12] L. Garrido,[39] C. Gaspar,[42] R. E. Geertsema,[32] D. Gerick,[17] L. L. Gerken,[15] E. Gersabeck,[56] M. Gersabeck,[56] T. Gershon,[50] L. Giambastiani,[28] V. Gibson,[49] H. K. Giemza,[36] A. L. Gilman,[57] M. Giovannetti,[23,t] A. Gioventù,[40] P. Gironella Gironell,[39] C. Giugliano,[21,j] K. Gizdov,[52] E. L. Gkougkousis,[42] V. V. Gligorov,[13,42] C. Göbel,[64] E. Golobardes,[74] D. Golubkov,[38] A. Golutvin,[55,38] A. Gomes,[1,b] S. Gomez Fernandez,[39] F. Goncalves Abrantes,[57] M. Goncerz,[35] G. Gong,[3] I. V. Gorelov,[38] C. Gotti,[26] J. P. Grabowski,[17] T. Grammatico,[13] L. A. Granado Cardoso,[42] E. Graugés,[39] E. Graverini,[43] G. Graziani, A. T. Grecu,[37] L. M. Greeven,[32] N. A. Grieser,[4] L. Grillo,[53] S. Gromov,[38] B. R. Gruberg Cazon,[57] C. Gu,[3] M. Guarise,[21,j] M. Guittiere,[11] P. A. Günther,[17] E. Gushchin,[38] A. Guth,[14] Y. Guz,[38] T. Gys,[42] T. Hadavizadeh,[63] G. Haefeli,[43] C. Haen,[42] J. Haimberger,[42] S. C. Haines,[49] T. Halewood-leagas,[54] M. M. Halvorsen,[42] P. M. Hamilton,[60] J. Hammerich,[54] Q. Han,[7] X. Han,[17] E. B. Hansen,[56] S. Hansmann-Menzemer,[17,42] L. Hao,[6] N. Harnew,[57] T. Harrison,[54] C. Hasse,[42] M. Hatch,[42] J. He,[6,d] K. Heijhoff,[32] K. Heinicke,[15] R. D. L. Henderson,[63,50] A. M. Hennequin,[58] K. Hennessy,[54] L. Henry,[42] J. Heuel,[14] A. Hicheur,[2] D. Hill,[43] M. Hilton,[56] S. E. Hollitt,[15] R. Hou,[7] Y. Hou,[8]

J. Hu,[17] J. Hu,[66] W. Hu,[7] X. Hu,[3] W. Huang,[6] X. Huang,[67] W. Hulsbergen,[32] R. J. Hunter,[50] M. Hushchyn,[38] D. Hutchcroft,[54] P. Ibis,[15] M. Idzik,[34] D. Ilin,[38] P. Ilten,[59] A. Inglessi,[38] A. Iniukhin,[38] A. Ishteev,[38] K. Ivshin,[38] R. Jacobsson,[42] H. Jage,[14] S. Jakobsen,[42] E. Jans,[32] B. K. Jashal,[41] A. Jawahery,[60] V. Jevtic,[15] X. Jiang,[4,6] M. John,[57] D. Johnson,[58] C. R. Jones,[49] T. P. Jones,[50] B. Jost,[42] N. Jurik,[42] S. Kandybei,[45] Y. Kang,[3] M. Karacson,[42] D. Karpenkov,[38] M. Karpov,[38] J. W. Kautz,[59] F. Keizer,[42] D. M. Keller,[62] M. Kenzie,[50] T. Ketel,[33] B. Khanji,[15] A. Kharisova,[38] S. Kholodenko,[38] T. Kirn,[14] V. S. Kirsebom,[43] O. Kitouni,[58] S. Klaver,[33] N. Kleijne,[29,q] K. Klimaszewski,[36] M. R. Kmiec,[36] S. Koliiev,[46] A. Kondybayeva,[38] A. Konoplyannikov,[38] P. Kopciewicz,[34] R. Kopecna,[17] P. Koppenburg,[32] M. Korolev,[38] I. Kostiuk,[32,46] O. Kot,[46] S. Kotriakhova, A. Kozachuk,[38] P. Kravchenko,[38] L. Kravchuk,[38] R. D. Krawczyk,[42] M. Kreps,[50] S. Kretzschmar,[14] P. Krokovny,[38] W. Krupa,[34] W. Krzemien,[36] J. Kubat,[17] W. Kucewicz,[35,34] M. Kucharczyk,[35] V. Kudryavtsev,[38] H. S. Kuindersma,[32] G. J. Kunde,[61] D. Lacarrere,[42] G. Lafferty,[56] A. Lai,[27] A. Lampis,[27,i] D. Lancierini,[44] J. J. Lane,[56] R. Lane,[48] G. Lanfranchi,[23] C. Langenbruch,[14] J. Langer,[15] O. Lantwin,[38] T. Latham,[50] F. Lazzari,[29,u] M. Lazzaroni,[25] R. Le Gac,[10] S. H. Lee,[76] R. Lefèvre,[9] A. Leflat,[38] S. Legotin,[38] P. Lenisa,[21,j] O. Leroy,[10] T. Lesiak,[35] B. Leverington,[17] H. Li,[66] K. Li,[7] P. Li,[17] S. Li,[7] Y. Li,[4] Z. Li,[62] X. Liang,[62] C. Lin,[6] T. Lin,[55] R. Lindner,[42] V. Lisovskyi,[15] R. Litvinov,[27,i] G. Liu,[66] H. Liu,[6] Q. Liu,[6] S. Liu,[4,6] A. Lobo Salvia,[39] A. Loi,[27] R. Lollini,[71] J. Lomba Castro,[40] I. Longstaff,[53] J. H. Lopes,[2] S. López Soliño,[40] G. H. Lovell,[49] Y. Lu,[4,c] C. Lucarelli,[22,k] D. Lucchesi,[28,o] S. Luchuk,[38] M. Lucio Martinez,[32] V. Lukashenko,[32,46] Y. Luo,[3] A. Lupato,[56] E. Luppi,[21,j] A. Lusiani,[29,q] K. Lynch,[18] X.-R. Lyu,[6] L. Ma,[4] R. Ma,[6] S. Maccolini,[20] F. Machefert,[11] F. Maciuc,[37] V. Macko,[43] P. Mackowiak,[15] S. Maddrell-Mander,[48] L. R. Madhan Mohan,[48] A. Maevskiy,[38] D. Maisuzenko,[38] M. W. Majewski,[34] J. J. Malczewski,[35] S. Malde,[57] B. Malecki,[35] A. Malinin,[38] T. Maltsev,[38] H. Malygina,[17] G. Manca,[27,i] G. Mancinelli,[10] D. Manuzzi,[20] C. A. Manzari,[44] D. Marangotto,[25,m] J. F. Marchand,[8] U. Marconi,[20] S. Mariani,[22,k] C. Marin Benito,[42] M. Marinangeli,[43] J. Marks,[17] A. M. Marshall,[48] P. J. Marshall,[54] G. Martelli,[71,p] G. Martellotti,[30] L. Martinazzoli,[42,n] M. Martinelli,[26,n] D. Martinez Santos,[40] F. Martinez Vidal,[41] A. Massafferri,[1] M. Materok,[14] R. Matev,[42] A. Mathad,[44] V. Matiunin,[38] C. Matteuzzi,[26] K. R. Mattioli,[76] A. Mauri,[32] E. Maurice,[12] J. Mauricio,[39] M. Mazurek,[42] M. McCann,[55] L. Mcconnell,[18] T. H. McGrath,[56] N. T. McHugh,[53] A. McNab,[56] R. McNulty,[18] J. V. Mead,[54] B. Meadows,[59] G. Meier,[15] D. Melnychuk,[36] S. Meloni,[26,n] M. Merk,[32,73] A. Merli,[25,m] L. Meyer Garcia,[2] M. Mikhasenko,[69,e] D. A. Milanes,[68] E. Millard,[50] M. Milovanovic,[42] M.-N. Minard,[8,8,a] A. Minotti,[26,m] S. E. Mitchell,[52] B. Mitreska,[56] D. S. Mitzel,[15] A. Mödden,[15] R. A. Mohammed,[57] R. D. Moise,[55] S. Mokhnenko,[38] T. Mombächer,[40] I. A. Monroy,[68] S. Monteil,[9] M. Morandin,[28] G. Morello,[23] M. J. Morello,[29,q] J. Moron,[34] A. B. Morris,[69] A. G. Morris,[50] R. Mountain,[62] H. Mu,[3] F. Muheim,[52] M. Mulder,[72] K. Müller,[44] C. H. Murphy,[57] D. Murray,[56] R. Murta,[55] P. Muzzetto,[27,i] P. Naik,[48] T. Nakada,[43] R. Nandakumar,[51] T. Nanut,[42] I. Nasteva,[2] M. Needham,[52] N. Neri,[25,m] S. Neubert,[69] N. Neufeld,[42] P. Neustroev,[38] R. Newcombe,[55] E. M. Niel,[43] S. Nieswand,[14] N. Nikitin,[38] N. S. Nolte,[58] C. Normand,[8,27,i] C. Nunez,[76] A. Oblakowska-Mucha,[34] V. Obraztsov,[38] T. Oeser,[14] D. P. O'Hanlon,[48] S. Okamura,[21,j] R. Oldeman,[27,i] F. Oliva,[52] M. E. Olivares,[62] C. J. G. Onderwater,[72] R. H. O'Neil,[52] J. M. Otalora Goicochea,[2] T. Ovsiannikova,[38] P. Owen,[44] A. Oyanguren,[41] O. Ozcelik,[52] K. O. Padeken,[69] B. Pagare,[50] P. R. Pais,[42] T. Pajero,[57] A. Palano,[19] M. Palutan,[23] Y. Pan,[56] G. Panshin,[38] A. Papanestis,[51] M. Pappagallo,[19,g] L. L. Pappalardo,[21,j] C. Pappenheimer,[59] W. Parker,[60] C. Parkes,[56] B. Passalacqua,[21,j] G. Passaleva,[22] A. Pastore,[19] M. Patel,[55] C. Patrignani,[20,h] C. J. Pawley,[73] A. Pearce,[42] A. Pellegrino,[32] M. Pepe Altarelli,[42] S. Perazzini,[20] D. Pereima,[38] A. Pereiro Castro,[40] P. Perret,[9] M. Petric,[53] K. Petridis,[48] A. Petrolini,[24,l] A. Petrov,[38] S. Petrucci,[52] M. Petruzzo,[25] H. Pham,[62] A. Philippov,[38] R. Piandani,[6] L. Pica,[29,q] M. Piccini,[71] B. Pietrzyk,[8] G. Pietrzyk,[11] M. Pili,[57] D. Pinci,[30] F. Pisani,[42] M. Pizzichemi,[26,42,n] V. Placinta,[37] J. Plews,[47] M. Plo Casasus,[40] F. Polci,[13,42] M. Poli Lener,[23] M. Poliakova,[62] A. Poluektov,[10] N. Polukhina,[38] I. Polyakov,[62] E. Polycarpo,[2] S. Ponce,[42] D. Popov,[6,42] S. Popov,[38] S. Poslavskii,[38] K. Prasanth,[35] L. Promberger,[42] C. Prouve,[40] V. Pugatch,[46] V. Puill,[11] G. Punzi,[29,r] H. R. Qi,[3] W. Qian,[6] N. Qin,[3] S. Qu,[3] R. Quagliani,[43] N. V. Raab,[18] R. I. Rabadan Trejo,[6] B. Rachwal,[34] J. H. Rademacker,[48] R. Rajagopalan,[62] M. Rama,[29] M. Ramos Pernas,[50] M. S. Rangel,[2] F. Ratnikov,[38] G. Raven,[33,42] M. Rebollo De Miguel,[41] M. Reboud,[8] F. Redi,[42] F. Reiss,[56] C. Remon Alepuz,[41] Z. Ren,[3] V. Renaudin,[57] P. K. Resmi,[10] R. Ribatti,[29,q]

A. M. Ricci,[27] S. Ricciardi,[51] K. Rinnert,[54] P. Robbe,[11] G. Robertson,[52] A. B. Rodrigues,[43] E. Rodrigues,[54] J. A. Rodriguez Lopez,[68] E. Rodriguez Rodriguez,[40] A. Rollings,[57] P. Roloff,[42] V. Romanovskiy,[38] M. Romero Lamas,[40] A. Romero Vidal,[40] J. D. Roth,[76,a] M. Rotondo,[23] M. S. Rudolph,[62] T. Ruf,[42] R. A. Ruiz Fernandez,[40] J. Ruiz Vidal,[41] A. Ryzhikov,[38] J. Ryzka,[34] J. J. Saborido Silva,[40] N. Sagidova,[38] N. Sahoo,[47] B. Saitta,[27,i] M. Salomoni,[42] C. Sanchez Gras,[32] I. Sanderswood,[41] R. Santacesaria,[30] C. Santamarina Rios,[40] M. Santimaria,[23] E. Santovetti,[31,t] D. Saranin,[38] G. Sarpis,[14] M. Sarpis,[69] A. Sarti,[30] C. Satriano,[30,s] A. Satta,[31] M. Saur,[15] D. Savrina,[38] H. Sazak,[9] L. G. Scantlebury Smead,[57] A. Scarabotto,[13] S. Schael,[14] S. Scherl,[54] M. Schiller,[53] H. Schindler,[42] M. Schmelling,[16] B. Schmidt,[42] S. Schmitt,[14] O. Schneider,[43] A. Schopper,[42] M. Schubiger,[32] S. Schulte,[43] M. H. Schune,[11] R. Schwemmer,[42] B. Sciascia,[23,42] A. Sciuccati,[42] S. Sellam,[40] A. Semennikov,[38] M. Senghi Soares,[33] A. Sergi,[24,l] N. Serra,[44] L. Sestini,[28] A. Seuthe,[15] Y. Shang,[5] D. M. Shangase,[76] M. Shapkin,[38] I. Shchemerov,[38] L. Shchutska,[43] T. Shears,[54] L. Shekhtman,[38] Z. Shen,[5] S. Sheng,[4,6] V. Shevchenko,[38] E. B. Shields,[26,n] Y. Shimizu,[11] E. Shmanin,[38] J. D. Shupperd,[62] B. G. Siddi,[21,j] R. Silva Coutinho,[44] G. Simi,[28] S. Simone,[19,g] M. Singla,[63] N. Skidmore,[56] R. Skuza,[17] T. Skwarnicki,[62] M. W. Slater,[47] I. Slazyk,[21,j] J. C. Smallwood,[57] J. G. Smeaton,[49] E. Smith,[44] M. Smith,[55] A. Snoch,[32] L. Soares Lavra,[9] M. D. Sokoloff,[59] F. J. P. Soler,[53] A. Solomin,[38,48] A. Solovev,[38] I. Solovyev,[38] F. L. Souza De Almeida,[2] B. Souza De Paula,[2] B. Spaan,[15,a] E. Spadaro Norella,[25,m] E. Spiridenkov,[38] P. Spradlin,[53] V. Sriskaran,[42] F. Stagni,[42] M. Stahl,[59] S. Stahl,[42] S. Stanislaus,[57] O. Steinkamp,[44] O. Stenyakin,[38] H. Stevens,[15] S. Stone,[62,a] D. Strekalina,[38] F. Suljik,[57] J. Sun,[27] L. Sun,[67] Y. Sun,[60] P. Svihra,[56] P. N. Swallow,[47] K. Swientek,[34] A. Szabelski,[36] T. Szumlak,[34] M. Szymanski,[42] S. Taneja,[56] A. R. Tanner,[48] M. D. Tat,[57] A. Terentev,[38] F. Teubert,[42] E. Thomas,[42] D. J. D. Thompson,[47] K. A. Thomson,[54] H. Tilquin,[55] V. Tisserand,[9] S. T'Jampens,[8] M. Tobin,[4] L. Tomassetti,[21,j] X. Tong,[5] D. Torres Machado,[1] D. Y. Tou,[3] E. Trifonova,[38] S. M. Trilov,[48] C. Trippl,[43] G. Tuci,[6] A. Tully,[43] N. Tuning,[32,42] A. Ukleja,[36] D. J. Unverzagt,[17] E. Ursov,[38] A. Usachov,[32] A. Ustyuzhanin,[38] U. Uwer,[17] A. Vagner,[38] V. Vagnoni,[20] A. Valassi,[42] G. Valenti,[20] N. Valls Canudas,[74] M. van Beuzekom,[32] M. Van Dijk,[43] H. Van Hecke,[61] E. van Herwijnen,[38] M. van Veghel,[72] R. Vazquez Gomez,[39] P. Vazquez Regueiro,[40] C. Vázquez Sierra,[42] S. Vecchi,[21] J. J. Velthuis,[48] M. Veltri,[22,v] A. Venkateswaran,[62] M. Veronesi,[32] M. Vesterinen,[50] D. Vieira,[59] M. Vieites Diaz,[43] X. Vilasis-Cardona,[74] E. Vilella Figueras,[54] A. Villa,[20] P. Vincent,[13] F. C. Volle,[11] D. vom Bruch,[10] A. Vorobyev,[38] V. Vorobyev,[38] N. Voropaev,[38] K. Vos,[73] R. Waldi,[17] J. Walsh,[29] C. Wang,[17] J. Wang,[5] J. Wang,[4] J. Wang,[3] J. Wang,[67] M. Wang,[5] R. Wang,[48] Y. Wang,[7] Z. Wang,[44] Z. Wang,[3] Z. Wang,[6] J. A. Ward,[50,63] N. K. Watson,[47] D. Websdale,[55] C. Weisser,[58] B. D. C. Westhenry,[48] D. J. White,[56] M. Whitehead,[53] A. R. Wiederhold,[50] D. Wiedner,[15] G. Wilkinson,[57] M. K. Wilkinson,[59] I. Williams,[49] M. Williams,[58] M. R. J. Williams,[52] F. F. Wilson,[51] W. Wislicki,[36] M. Witek,[35] L. Witola,[17] C. P. Wong,[61] G. Wormser,[11] S. A. Wotton,[49] H. Wu,[62] K. Wyllie,[42] Z. Xiang,[6] D. Xiao,[7] Y. Xie,[7] A. Xu,[5] J. Xu,[6] L. Xu,[3] M. Xu,[50] Q. Xu,[6] Z. Xu,[9] Z. Xu,[6] D. Yang,[3] S. Yang,[6] Y. Yang,[6] Z. Yang,[5] Z. Yang,[60] Y. Yao,[62] L. E. Yeomans,[54] H. Yin,[7] J. Yu,[65] X. Yuan,[62] E. Zaffaroni,[43] M. Zavertyaev,[16] M. Zdybal,[35] O. Zenaiev,[42] M. Zeng,[3] D. Zhang,[7] L. Zhang,[3] S. Zhang,[65] S. Zhang,[5] Y. Zhang,[5] Y. Zhang,[57] A. Zharkova,[38] A. Zhelezov,[17] Y. Zheng,[6] T. Zhou,[5] X. Zhou,[6] Y. Zhou,[6] V. Zhovkovska,[11] X. Zhu,[3] X. Zhu,[7] Z. Zhu,[6] V. Zhukov,[14,38] Q. Zou,[4,6] S. Zucchelli,[20,h] D. Zuliani,[28] and G. Zunica[56]

(LHCb Collaboration)

[1]*Centro Brasileiro de Pesquisas Físicas (CBPF), Rio de Janeiro, Brazil*
[2]*Universidade Federal do Rio de Janeiro (UFRJ), Rio de Janeiro, Brazil*
[3]*Center for High Energy Physics, Tsinghua University, Beijing, China*
[4]*Institute Of High Energy Physics (IHEP), Beijing, China*
[5]*School of Physics State Key Laboratory of Nuclear Physics and Technology, Peking University, Beijing, China*
[6]*University of Chinese Academy of Sciences, Beijing, China*
[7]*Institute of Particle Physics, Central China Normal University, Wuhan, Hubei, China*
[8]*Université Savoie Mont Blanc, CNRS, IN2P3-LAPP, Annecy, France*
[9]*Université Clermont Auvergne, CNRS/IN2P3, LPC, Clermont-Ferrand, France*

[10]*Aix Marseille Univ, CNRS/IN2P3, CPPM, Marseille, France*
[11]*Université Paris-Saclay, CNRS/IN2P3, IJCLab, Orsay, France*
[12]*Laboratoire Leprince-Ringuet, CNRS/IN2P3, Ecole Polytechnique, Institut Polytechnique de Paris, Palaiseau, France*
[13]*LPNHE, Sorbonne Université, Paris Diderot Sorbonne Paris Cité, CNRS/IN2P3, Paris, France*
[14]*I. Physikalisches Institut, RWTH Aachen University, Aachen, Germany*
[15]*Fakultät Physik, Technische Universität Dortmund, Dortmund, Germany*
[16]*Max-Planck-Institut für Kernphysik (MPIK), Heidelberg, Germany*
[17]*Physikalisches Institut, Ruprecht-Karls-Universität Heidelberg, Heidelberg, Germany*
[18]*School of Physics, University College Dublin, Dublin, Ireland*
[19]*INFN Sezione di Bari, Bari, Italy*
[20]*INFN Sezione di Bologna, Bologna, Italy*
[21]*INFN Sezione di Ferrara, Ferrara, Italy*
[22]*INFN Sezione di Firenze, Firenze, Italy*
[23]*INFN Laboratori Nazionali di Frascati, Frascati, Italy*
[24]*INFN Sezione di Genova, Genova, Italy*
[25]*INFN Sezione di Milano, Milano, Italy*
[26]*INFN Sezione di Milano-Bicocca, Milano, Italy*
[27]*INFN Sezione di Cagliari, Monserrato, Italy*
[28]*Università degli Studi di Padova, Università e INFN, Padova, Padova, Italy*
[29]*INFN Sezione di Pisa, Pisa, Italy*
[30]*INFN Sezione di Roma La Sapienza, Roma, Italy*
[31]*INFN Sezione di Roma Tor Vergata, Roma, Italy*
[32]*Nikhef National Institute for Subatomic Physics, Amsterdam, Netherlands*
[33]*Nikhef National Institute for Subatomic Physics and VU University Amsterdam, Amsterdam, Netherlands*
[34]*AGH—University of Science and Technology, Faculty of Physics and Applied Computer Science, Kraków, Poland*
[35]*Henryk Niewodniczanski Institute of Nuclear Physics Polish Academy of Sciences, Kraków, Poland*
[36]*National Center for Nuclear Research (NCBJ), Warsaw, Poland*
[37]*Horia Hulubei National Institute of Physics and Nuclear Engineering, Bucharest-Magurele, Romania*
[38]*Affiliated with an institute covered by a cooperation agreement with CERN*
[39]*ICCUB, Universitat de Barcelona, Barcelona, Spain*
[40]*Instituto Galego de Física de Altas Enerxías (IGFAE), Universidade de Santiago de Compostela, Santiago de Compostela, Spain*
[41]*Instituto de Fisica Corpuscular, Centro Mixto Universidad de Valencia—CSIC, Valencia, Spain*
[42]*European Organization for Nuclear Research (CERN), Geneva, Switzerland*
[43]*Institute of Physics, Ecole Polytechnique Fédérale de Lausanne (EPFL), Lausanne, Switzerland*
[44]*Physik-Institut, Universität Zürich, Zürich, Switzerland*
[45]*NSC Kharkiv Institute of Physics and Technology (NSC KIPT), Kharkiv, Ukraine*
[46]*Institute for Nuclear Research of the National Academy of Sciences (KINR), Kyiv, Ukraine*
[47]*University of Birmingham, Birmingham, United Kingdom*
[48]*H.H. Wills Physics Laboratory, University of Bristol, Bristol, United Kingdom*
[49]*Cavendish Laboratory, University of Cambridge, Cambridge, United Kingdom*
[50]*Department of Physics, University of Warwick, Coventry, United Kingdom*
[51]*STFC Rutherford Appleton Laboratory, Didcot, United Kingdom*
[52]*School of Physics and Astronomy, University of Edinburgh, Edinburgh, United Kingdom*
[53]*School of Physics and Astronomy, University of Glasgow, Glasgow, United Kingdom*
[54]*Oliver Lodge Laboratory, University of Liverpool, Liverpool, United Kingdom*
[55]*Imperial College London, London, United Kingdom*
[56]*Department of Physics and Astronomy, University of Manchester, Manchester, United Kingdom*
[57]*Department of Physics, University of Oxford, Oxford, United Kingdom*
[58]*Massachusetts Institute of Technology, Cambridge, MA, United States*
[59]*University of Cincinnati, Cincinnati, OH, United States*
[60]*University of Maryland, College Park, MD, United States*
[61]*Los Alamos National Laboratory (LANL), Los Alamos, NM, United States*
[62]*Syracuse University, Syracuse, NY, United States*
[63]*School of Physics and Astronomy, Monash University, Melbourne, Australia (associated with Department of Physics, University of Warwick, Coventry, United Kingdom)*
[64]*Pontifícia Universidade Católica do Rio de Janeiro (PUC-Rio), Rio de Janeiro, Brazil (associated with Universidade Federal do Rio de Janeiro (UFRJ), Rio de Janeiro, Brazil)*

[65]*Physics and Micro Electronic College, Hunan University, Changsha City, China (associated with Institute of Particle Physics, Central China Normal University, Wuhan, Hubei, China)*
[66]*Guangdong Provincial Key Laboratory of Nuclear Science, Guangdong-Hong Kong Joint Laboratory of Quantum Matter, Institute of Quantum Matter, South China Normal University, Guangzhou, China (associated with Center for High Energy Physics, Tsinghua University, Beijing, China)*
[67]*School of Physics and Technology, Wuhan University, Wuhan, China (associated with Center for High Energy Physics, Tsinghua University, Beijing, China)*
[68]*Departamento de Fisica, Universidad Nacional de Colombia, Bogota, Colombia (associated with LPNHE, Sorbonne Université, Paris Diderot Sorbonne Paris Cité, CNRS/IN2P3, Paris, France)*
[69]*Universität Bonn—Helmholtz-Institut für Strahlen und Kernphysik, Bonn, Germany (associated with Physikalisches Institut, Ruprecht-Karls-Universität Heidelberg, Heidelberg, Germany)*
[70]*Eotvos Lorand University, Budapest, Hungary (associated with European Organization for Nuclear Research (CERN), Geneva, Switzerland)*
[71]*INFN Sezione di Perugia, Perugia, Italy (associated with INFN Sezione di Bari, Bari, Italy)*
[72]*Van Swinderen Institute, University of Groningen, Groningen, Netherlands (associated with Nikhef National Institute for Subatomic Physics, Amsterdam, Netherlands)*
[73]*Universiteit Maastricht, Maastricht, Netherlands (associated with Nikhef National Institute for Subatomic Physics, Amsterdam, Netherlands)*
[74]*DS4DS, La Salle, Universitat Ramon Llull, Barcelona, Spain (associated with ICCUB, Universitat de Barcelona, Barcelona, Spain)*
[75]*Department of Physics and Astronomy, Uppsala University, Uppsala, Sweden (associated with School of Physics and Astronomy, University of Glasgow, Glasgow, United Kingdom)*
[76]*University of Michigan, Ann Arbor, MI, United States (associated with Syracuse University, Syracuse, NY, United States)*

[a]Deceased.
[b]Also at Universidade Federal do Triângulo Mineiro (UFTM), Uberaba-MG, Brazil.
[c]Also at Central South U., Changsha, China.
[d]Also at Hangzhou Institute for Advanced Study, UCAS, Hangzhou, China.
[e]Also at Excellence Cluster ORIGINS, Munich, Germany.
[f]Also at Universidad Nacional Autónoma de Honduras, Tegucigalpa, Honduras.
[g]Also at Università di Bari, Bari, Italy.
[h]Also at Università di Bologna, Bologna, Italy.
[i]Also at Università di Cagliari, Cagliari, Italy.
[j]Also at Università di Ferrara, Ferrara, Italy.
[k]Also at Università di Firenze, Firenze, Italy.
[l]Also at Università di Genova, Genova, Italy.
[m]Also at Università degli Studi di Milano, Milano, Italy.
[n]Also at Università di Milano Bicocca, Milano, Italy.
[o]Also at Università di Padova, Padova, Italy.
[p]Also at Università di Perugia, Perugia, Italy.
[q]Also at Scuola Normale Superiore, Pisa, Italy.
[r]Also at Università di Pisa, Pisa, Italy.
[s]Also at Università della Basilicata, Potenza, Italy.
[t]Also at Università di Roma Tor Vergata, Roma, Italy.
[u]Also at Università di Siena, Siena, Italy.
[v]Also at Università di Urbino, Urbino, Italy.